Experimental simulation of bubble nucleation and magma ascent in basaltic systems: Implications for Stromboli volcano — Source link [↗]

Nolwenn Le Gall, Michel Pichavant

Institutions: University of Orléans

Related papers:

- Homogeneous bubble nucleation in H2O- and H2O-CO2-bearing basaltic melts: results of high temperature decompression experiments

- Generation of CO2-rich melts during basalt magma ascent and degassing

- Experimental study of bubble growth in Stromboli basalt melts at 1 atm

- Delayed, disequilibrium degassing in rhyolite magma: Decompression experiments and implications for explosive volcanism

- Degassing of hydrous trachytic Campi Flegrei and phonolitic Vesuvius melts: Experimental limitations and chances to study homogeneous bubble nucleation

Experimental simulation of bubble nucleation and magma ascent in basaltic systems : implications for Stromboli volcano.

Nolwenn Le Gall, Michel Pichavant

Experimental simulation of bubble nucleation and magma ascent in basaltic systems: Implications for Stromboli volcano

Nolwenn Le Gall[1,*] and Michel Pichavant[1]

[1]Université d'Orléans, ISTO, UMR 7327, 45071, Orléans, France, and CNRS/INSU, ISTO, UMR 7327, 45071, Orléans, France, and BRGM, ISTO, UMR 7327, BP 36009, 45060, Orléans, France

Abstract

The ascent of H_2O- and H_2O-CO_2-bearing basaltic melts from the deeper to the shallower part of the Stromboli magmatic system and their vesiculation were simulated from decompression experiments. A well-studied "golden" pumice produced during an intermediate- to a large-scale paroxysm was used as starting material. Volatile-bearing glasses were synthesized at an oxygen fugacity (f_{O_2}) ranging from NNO–1.4 to +0.9, 1200 °C and 200 MPa. The resulting crystal- and bubble-free glasses were then isothermally (1200 °C) decompressed to final pressures P_f ranging between 200 and 25 MPa, at a linear ascent rate of 1.5 m/s (or 39 kPa/s) prior to be rapidly quenched. Textures of post-decompression glasses that were characterized by X-ray computed tomography result from different mechanisms of degassing that include bubble nucleation, growth, coalescence, and outgassing, as well as fragmentation. Homogeneous bubble nucleation occurs for supersaturation pressures (difference between saturation pressure and pressure at which bubbles start to form homogeneously, ΔP_{HoN}) ≤ 50 MPa. In the CO_2-free melts, homogeneous nucleation occurs as two distinct events, the first at high P_f (200–150 MPa) and the second at low P_f (50–25 MPa) near the fragmentation level. In contrast, in the CO_2-bearing melts, multiple events of homogeneous bubble nucleation occur over a substantial P_f interval along the decompression path. Bubble coalescence occurs in both H_2O- and H_2O-CO_2-bearing melts and is the more strongly marked between 100 and 50 MPa P_f. The CO_2-free melts follow equilibrium degassing until 100 MPa P_f and are slightly supersaturated at 60 and 50 MPa P_f, thus providing the driving force for the second bubble nucleation event. In comparison, disequilibrium degassing occurs systematically in the CO_2-bearing melts that retain high CO_2 concentrations. Fragmentation was observed in some CO_2-free charges decompressed to 25 MPa P_f and is intimately associated with the occurrence of the second bubble nucleation event. Textures of H_2O-CO_2-bearing glasses reproduce certain critical aspects of the Stromboli natural textures (bubble number densities, shapes, sizes, and distributions) and chemistries (residual volatile concentrations). Average bubble sizes, bubble size distribution (BSD), and bubble number density (BND) data are used together to estimate that the "golden" pumice magmas ascend from their source region in 43 to 128 min.

Keywords: Basalt, Stromboli, volatiles, magma degassing, magma ascent, bubble nucleation, fragmentation

Introduction

Water and carbon dioxide, which are the two main volatile components dissolved in basalt magmas, control the physical processes involved in volcanic eruptions (e.g., Cashman and Sparks 2013). As magma ascends to the Earth's surface, pressure decreases and this causes exsolution of the dissolved volatiles from the supersaturated melt. Accordingly, gas bubbles nucleate, grow, and coalesce as magma continues to ascend. The evolution of the gas phase within the volcanic conduit is thought to govern the eruptive behavior. The gas phase can either remain as bubbles within the melt ("closed-system" degassing) or escape from the magma ("open-system" degassing). The former case would lead to explosive behavior and the latter to effusive

behavior (e.g., Gonnermann and Manga 2005, 2007). As an illustration, Stromboli volcano (Aeolian Islands, Italy) is, among other basaltic volcanoes, characterized by various eruptive styles ranging from lava flows to mild Strombolian explosions to more violent explosions. Such a variety is thought to be controlled by the kinetics of magma vesiculation (bubble nucleation, growth, and coalescence) and fragmentation, as well as by changes in magma ascent rate (Woods and Koyaguchi 1994; Sparks 2003; Edmonds 2008).

Studies of when and how gas bubbles form and separate from magma are needed to better understand whether a volcanic eruption is effusive or explosive (Edmonds 2008). Volcanic magma degassing, corresponding to the loss of dissolved volatiles, can be studied from different approaches. The first, including petrological studies and phase equilibria experiments, aims at determining the volatile compositions and concentrations in magma prior to significant degassing (Edmonds 2008) (e.g., Bertagnini et al.

2003; Métrich et al. 2005, 2010; Di Carlo et al. 2006; Pichavant et al. 2009, 2011). Volatile solubility models (e.g., Newman and Lowenstern 2002; Papale et al. 2006; Iacono-Marziano et al. 2012) play an important role. The second, including textural and geochemical studies, deals with the exsolved, integrated products of degassing (Edmonds 2008) (e.g., Mangan and Cashman 1996; Gaonac'h et al. 1996; Lautze and Houghton 2007; Polacci et al. 2006, 2008, 2009; Burton et al. 2007; Allard 2010; Aiuppa et al. 2010a, 2011). In addition, numerical models are becoming available to simulate the physical (textures) and chemical (volcanic gases, volatile solubilities) evolution of gas bubbles and melt during degassing (e.g., Blower et al. 2001, 2002; Toramaru 2006; Burgisser et al. 2015). However, none of these two main approaches are completely satisfactory. Volatile solubility models as well as the interpretation of volcanic gas data assume gas-melt equilibrium degassing of basaltic magmas, while recent experiments (Pichavant et al. 2013; Le Gall and Pichavant 2016) have reported the possibility of disequilibrium degassing during ascent and decompression of CO_2-bearing basaltic melts. There are also problems and disagreements associated with the interpretation of textural and chemical data in natural eruption products (Gaonac'h et al. 1996; Blower et al. 2001, 2002; Edmonds 2008).

In complement to these two main approaches, high-pressure and temperature-decompression experiments (e.g., Hurwitz and Navon 1994; Gardner et al. 1999; Mourtada-Bonnefoi and Laporte 1999; Mangan and Sisson 2000, 2005; Mourtada-Bonnefoi and Laporte 2002, 2004; Iacono-Marziano et al. 2007; Cluzel et al. 2008; Gardner and Ketcham 2011) have the advantage to simulate the vesiculation process during magma ascent. Therefore, in an attempt to assist in the interpretation of textural and chemical data collected on basaltic eruptive products, we performed experimental simulations of the ascent and degassing of H_2O- and H_2O-CO_2-bearing Stromboli melts. The run products were texturally and chemically characterized to model the behavior of the major volatiles (H_2O, CO_2) during decompression and, in particular, to assess the effect of ascent rate on the degassing kinetics. Our results bring direct constraints on degassing processes at Stromboli, which is one representative example of explosive basaltic volcanoes (Rosi et al. 2013). It is also a very well-studied system and melt inclusion data (e.g., Bertagnini et al. 2003; Métrich et al. 2005, 2010) and gas measurements (e.g., Burton et al. 2007; Aiuppa et al. 2010a, 2010b, 2011; La Spina et al. 2013) are available. In addition, H_2O and CO_2 solubility data (both models and experiments, Newman and Lowenstern 2002; Shishkina et al. 2010; Lesne et al. 2011a, 2011b) allow detailed interpretation of natural products.

VOLCANOLOGICAL BACKGROUND

Stromboli is a basaltic volcano located in the Aeolian Islands, Italy. It is well known for its persistent explosive activity established 1300–1700 yr ago (Rosi et al. 2000). This normal activity, which consists of rhythmic, mild to moderate explosions lasting a few seconds (e.g., Rosi et al. 2013) is associated with a continuous degassing dominated by H_2O, CO_2, and SO_2 (Aiuppa et al. 2010a). Every 10–20 min, scoriaceous lapilli and bombs, ash, and lithic blocks are ejected to heights of a few tens to hundreds of meters above the summit craters (Rosi et al. 2000; Bertagnini et al. 2003; Francalanci et al. 2004). According to Burton et al. (2007),

such explosions result from the buoyant rise of deep-sourced (<3 km) gas slugs. This normal Strombolian activity can be suddenly interrupted by lava flows, and by violent explosions of variable scale defined as Strombolian paroxysms (Mercalli 1907; Rosi et al. 2013). Paroxysms range from small-scale (Métrich et al. 2005; Bertagnini et al. 2008; Rosi et al. 2013), also designated as "major explosions" (Barberi et al. 1993), to large-scale, the latter often called paroxysms for simplicity (Bertagnini et al. 2011; Rosi et al. 2013). These more violent explosions occur at a rate from 1.7 episodes per year (Rosi et al. 2013) to 1–10 episodes per century (Pichavant et al. 2009). During these highly energetic events, fallouts of meter-sized bombs and blocks, gas and ash, are produced and ejected up to a few kilometers from the vents.

These three types of eruptive activity at Stromboli are fed by two distinct magmas: a volatile-poor black scoria and a volatile-rich yellowish pumice (designated as "golden" pumice; Métrich et al. 2001; Bertagnini et al. 2003, 2008). The former, which supplies normal Strombolian activity and lava flows, is highly porphyritic (~50 vol% crystals of plagioclase, clinopyroxene, and olivine; Landi et al. 2004; Pichavant et al. 2011). In contrast, the latter, commonly produced during the paroxysms, has low porphyricity (~10 vol% crystals of clinopyroxene, olivine, and plagioclase; e.g., Francalanci et al. 2004; Pichavant et al. 2011). The present-day feeding system is thought to comprise a shallow reservoir hosting the black scoria magmas, recharged with the periodic arrival of "golden" pumice magmas from a deeper crustal reservoir (Pichavant et al. 2009, 2011; Métrich et al. 2010). Both magmas are often intermingled, and crystals in the "golden" pumices mainly come from the black scoria because of syn-eruptive mingling between the two magma types (e.g., Di Carlo et al. 2006).

Strombolian paroxysms constitute a serious hazard for inhabitants and visitors, due to their high intensity and potential to strike inhabited areas (Rosi et al. 2013). Development of the monitoring system because the 2002–2003 crisis now allows to daily collect a large body of geochemical and geophysical data (e.g., Ripepe and Harris 2008; Rosi et al. 2013). Continuous measurements of CO_2 and SO_2 emissions have evidenced significant changes in the chemical composition of the gases between quiescent, passive degassing and eruptions (Burton et al. 2007; Aiuppa et al. 2009, 2010a, 2010b, 2011; La Spina et al. 2013). Concerning Strombolian paroxysms, these appear systematically preceded by medium-term (days to weeks) increases of CO_2 fluxes (Aiuppa et al. 2010a, 2010b, 2011). Two main models have been proposed to explain these observations. According to Bertagnini et al. (2003) and Métrich et al. (2001, 2005, 2010), the more violent explosions would be generated by the rapid ascent, decompression, and fragmentation of a volatile-rich, low-porphyritic magma ("golden" pumice) batch. Alternatively, Allard (2010) suggests that such events would result from the bursting of CO_2-rich gas slugs generated at 8–10 km depth. In addition, Pichavant et al. (2013) have proposed that Strombolian paroxysms would be driven by explosive degassing and fragmentation of CO_2-oversaturated melts produced as a result of disequilibrium degassing during ascent.

EXPERIMENTAL METHODS

Two types of experiments were performed: synthesis and decompression. The synthesis experiments were conducted to generate the bubble-free H_2O- and H_2O-CO_2-bearing basaltic melts to be used in the decompression experiments, to simulate their ascent.

Scaling of the decompression experiments

Experimental conditions (P, T, basaltic composition, dissolved H_2O/CO_2, ascent rate, and f_{O_2}) were scaled against Stromboli. In this way, the initial pressure ($P_{in} = 200$ MPa) chosen in the decompression experiments is consistent with the depth of the storage region of "golden" pumice melts (around 7.5 km, Di Carlo et al. 2006; Pichavant et al. 2009; Métrich et al. 2010). Final pressures ($P_f = 200$–25 MPa) correspond to different heights in the volcanic conduit. The temperature ($T = 1200$ °C and kept constant) was chosen to be above the liquidus of "golden" pumice melts, on the basis of previous phase-equilibrium experiments (Di Carlo et al. 2006; Pichavant et al. 2009). All experiments were performed with the same basaltic composition representative of "golden" pumice melts involved in the present-day activity at Stromboli (Francalanci et al. 1989,1993, 2004; Di Carlo et al. 2006). The pre-decompression ranges of volatile concentrations (0.71–4.94 wt% H_2O, 818–1094 ppm CO_2) investigated overlap with the H_2O and CO_2 concentrations in Stromboli melt inclusions (e.g., Métrich et al. 2010). Concerning the ascent rate, there is a large uncertainty on Stromboli. On the one hand, an ascent rate of 3 mm/s (Calvari et al. 2011) implies that "golden" magmas would ascend from 7–8 km depth in about 1 month. This seems much too slow because "golden" pumices lack microlites, which implies ascent durations of a maximum of 10 h (Di Carlo et al. 2006; Pichavant et al. 2011). On the other hand, an ascent velocity of 32 m/s has been proposed from Stromboli melt viscosity data (Misiti et al. 2009), implying an ascent time of only a few minutes from 7–8 km depth. In this study an average ascent rate value of 1.5 m/s was investigated more in line with the petrological constraints (<10 h). This value is in the average of ascent rates determined for Vulcanello shoshonite magmas (0.27–3.2 m/s; Vetere et al. 2007), a system closely similar to that of Stromboli (Pichavant et al. 2013). Concerning the redox state, oxidizing redox conditions around ΔNNO = +0.5 (where NNO is the nickel-nickel oxide buffer) were determined for the near-liquidus evolution of "golden" pumice melts (Di Carlo et al. 2006; Pichavant et al. 2009) and this f_{O_2} range was imposed in our decompression experiments.

Starting material

The starting material used for the experiments is a high-K basalt from a paroxysmal explosion (PST-9 "golden" pumice, Di Carlo et al. 2006; Pichavant et al. 2009, 2011). The whole-rock composition of this pumice sample is shown in Table 1. PST-9 is highly vesicular (~60 vol% vesicles) and slightly porphyritic (~11 vol%; Pichavant et al. 2011), within the range of other pumices. A homogeneous starting glass was obtained by crushing the PST-9 pumice and melting the fine powder at 1400 °C, 1 atm, during 3 h, in a Pt crucible (Table 1). The resulting crystal- and bubble-free glass was then cored to cylinders with a diameter of 2.5 and, less frequently, 5 mm and typical lengths around 10 and 6 mm, respectively. The 5 mm diameter was tested to explore the influence of sample size on bubble nucleation.

For the synthesis experiments (Table 2), the glass cylinders were loaded into capsules (1.5–3 cm length, 2.5 or 5 mm internal diameter, 0.2 wall thickness) made of $Au_{80}Pd_{20}$. Such a metal composition was used to minimize iron loss during the experiments (Di Carlo et al. 2006; Pichavant et al. 2009). Distilled water and carbon dioxide as silver oxalate ($Ag_2C_2O_4$) were used as volatile sources. Three different

proportions of H_2O and CO_2 were introduced in the capsules, corresponding to $X_{H_2O_{in}}$ [molar $H_2O/(H_2O+CO_2)$] = 1 (series #1: only H_2O dissolved in glass, no CO_2 present), 0.25–0.56 (series #2: H_2O and CO_2 both dissolved in glass, high dissolved H_2O/CO_2), and 0 (series #3: H_2O and CO_2 both dissolved in glass, low dissolved H_2O/CO_2, see below for the origin of H_2O). For the 5 mm diameter cores, only $X_{H_2O_{in}} = 1$ conditions were investigated, because homogenization of melt CO_2 concentrations would have required a prohibitively long experimental duration (Zhang and Ni 2010). In one of the synthesis experiments (S5, Table 2), a separate Ni-NiPd sensor capsule was included for the determination of the experimental f_{H_2}. It consisted of two pellets of NiPd metal mixtures (with different Ni/Pd ratio) plus NiO, placed in a Pt capsule in the presence of excess H_2O (Taylor et al. 1992).

For the decompression experiments (Table 3), the synthesized volatile-bearing glass cores (2.5 or 5 mm in diameter and about 4 mm long) were fitted into $Au_{80}Pd_{20}$ capsules without further addition of volatiles. Capsules of identical internal diameter (2.5 and 5 mm) but variable lengths (from 1 to 5 cm for the capsules decompressed to the lowest pressures) were used to accommodate gas expansion during decompression.

Capsules were weighed before and after welding to ensure that no leaks occurred.

Equipment

All experiments were carried out in an internally heated pressure vessel (IHPV), working vertically and equipped with a rapid-quench device. The vessel was pressurized with Ar-H_2 mixtures obtained by sequential loading of H_2 and Ar at room temperature (Scaillet et al. 1992). The synthesis and decompression experiments were performed with an initial H_2 pressure of 1 bar and experimental f_{H_2} measured in one run with a redox sensor (see above). Then, Ar was pumped into the IHPV up to the pressure needed to attain the final target conditions (Pichavant et al. 2013). Total pressure was recorded continuously by a transducer calibrated against a Heise gauge with an accuracy of ±20 bars. The capsules were placed together in a sample holder made of an alumina tube and suspended by a thin Pt wire in a molybdenum furnace having a 2–3 cm long hotspot. Temperature was measured using two S-type thermocouples placed along the length of the capsules and recorded continuously (uncertainty ±5 °C) with a Eurotherm controller. Near-isothermal conditions (gradient <2–3 °C/cm) were maintained in the sample holder. At the end of the synthesis and decompression experiments, the Pt suspension wire was fused electrically, allowing the sample holder to fall into the cold part of the vessel, leading to a cooling rate of about 100 °C/s (Di Carlo et al. 2006).

Run procedure

All synthesis and decompression experiments were performed independently from each other.

The synthesis experiments were performed at 200 MPa and 1200 °C (Table 2),

TABLE 1. Composition of PST-9 golden pumice and starting glass

Label	PST-9[a]	Glass[b] ($n = 54$)
SiO_2	49.4	50.9(3)[c]
TiO_2	0.79	0.81(8)
Al_2O_3	15.75	15.99(28)
Fe_2O_3	1.3	nd
FeO	6.5	7.7(6)[d]
MnO	0.15	0.16(8)
MgO	7.96	7.21(41)
CaO	12.73	12.34(24)
Na_2O	2.27	2.39(9)
K_2O	1.85	1.90(12)
P_2O_5	0.43	0.55(17)
Cr_2O_3	–	0.03(4)
NiO	–	0.05(6)
Total	99.1	97.4(10)

Notes: Oxides are in wt%. nd = not determined.
[a] Whole-rock analysis performed at CRPG, Nancy, France (from Di Carlo et al. 2006).
[b] Electron microprobe analysis (normalized to 100%) of PST-9 glass (from Le Gall and Pichavant 2016), n = number of analyses.
[c] One standard deviation in terms of last digit.
[d] Total Fe as FeO.

TABLE 2. Synthesis experiments

Run	$X_{H_2O_{in}}$	T (°C)	P (MPa)	t (min)	H_2O glass (wt%)	CO_2 glass (ppm)
Volatile: H_2O (no. 1)						
S3#1	1	1200	202.2	2793	4.91(3)	0(0)
S4#1	1	1200	203.1	2509	4.93(5)	0(0)
S5#1	1	1200	202.8	2985	4.94(4)	0(0)
S6#1	1	1200	202.2	2760	4.90(1)	0(0)
S8#1	1	1200	203.8	4198	2.53(5)	0(0)
S11#1	1	1200	202.1	2900	4.90(3)	0(0)
S14#1	1	1200	201.9	1465	4.91(1)	0(0)
S16#1	1	1200	201.8	2873	4.90(2)	0(0)
Volatile: H_2O+CO_2 (no. 2)						
S3#2	0.25	1200	202.2	2793	1.95(1)	818(111)
S4#2	0.55	1200	203.1	2509	[a]0.58(1)	864(17)
S6#2	0.56	1200	202.2	2760	2.37(1)	1011(106)
Volatile: H_2O+CO_2 (no. 3)						
S3#3	0	1200	202.2	2793	1.12(1)	840(92)
S4#3	0	1200	203.1	2509	0.71(1)	860(78)
S5#3	0	1200	202.8	2985	0.84(4)	1063(109)
S6#3	0	1200	202.2	2760	0.80(3)	852(57)
S8#3	0	1200	203.8	4198	0.79(1)	1094(56)
S13#3	0	1200	201.5	2878	1.09(3)	923(132)

Notes: S11 synthesis from Le Gall (2015). $X_{H_2O_{in}}$ = initial molar $H_2O/(H_2O+CO_2)$ in the charge. T = run temperature; P = run pressure; t = duration of the synthesis experiment.
[a] ~2.50 wt% H_2O (see text for explanation).

TABLE 3. Decompression experiments: Run conditions and textural information

Sample	Starting glass	P_{in} (MPa)	P_f (MPa)	t_{ramp} (s)	$\|dP/dt\|$ (kPa/s)	Bubble 3D characteristics										
						n	peak size (µm)	range (µm)	D (µm)	BND^a (mm^{-3})	BND_{melt}^b (mm^{-3})	S (µm)	V^c (vol%)	V^d (vol%)	$V_{Equi.H_2O}$ (vol%)	$V_{Equi.CO_2}$ (vol%)
						Volatile: H$_2$O (no. 1)										
D3#1	S5#1	200	200	0	39	0	–	–	0(0)^g	0.00	0.00	–	0.00	0.00(0)	0.00	
D30#1	S16#1	200	150	1284	39	8350	6	4–46	8(3)	1324	1325	56	0.06	0.05(0)	9.22	
D2#1	S3#1	200	99.8	2568	39	42	29	9–120	58(28)	7.97	7.98	310	0.14	0.28(0.1)	24.1	
D22#1	S14#1	200	60	3649	39	149	–	15–266	121(67)	2.51	2.52	456	0.45	2.10(1.5)	44.3	
D5#1	S4#1	200	50	3840	39	5	–	40–200	113(58)	1.33	1.33	564	0.17	0.31(0.3)	51.0	
D8#1	S8#1	200	25	4488	39	567	27	7–73	28(11)	397	400	84	0.64	1.45(0.2)	72.5	
D19#1	S6#1	200	25	4488	39	nd	nd	nd	nd	nd	nd	nd	nd	nd	72.5	
D24#1^e	S11#1	200	25	4488	39	> 28	nd	400–1800	741	0.65	0.76	680	0.00	71.2(1.8)	72.5	
D24#1^f	S11#1	200	25	4488	39	58	10	9–56	17(10)	6.89	6.89	326	0.00	71.2(1.8)	72.5	
						Volatile: H$_2$O+CO$_2$ (no. 2)										
D3#2	S4#2	200	200	0	39	10	19	6–141	40(43)	1.15	1.15	592	0.02	0.05(0)	0.00	0.00
D1#2	S3#2	200	149.9	1284	39	15	6–7	6–60	13(14)	1.95	1.95	497	0.00	0.01(0)	9.22	0.17
D2#2	S3#2	200	99.8	2568	39	665	15	15–48	19(4)	104	105	132	0.04	0.10(0)	24.1	0.47
D5#2	S4#2	200	50	3840	39	114	15	6–73	17(11)	19.2	19.2	232	0.01	0.04(0)	51.0	1.48
D6#2	S6#2	200	25	4488	39	179	53	21–179	69(33)	152	159	115	4.70	12.6(2.7)	72.5	3.47
D8#2	S6#2	200	25	4488	39	171	61, 97	24–175	74(28)	186	198	107	5.82	13.8(2)	72.5	3.47
						Volatile: H$_2$O+CO$_2$ (no. 3)										
D3#3	S4#3	200	200	0	39	0	–	–	0(0)	0.00	0.00	–	0.00	0.00(0)	0.00	0.00
D1#3	S3#3	200	149.9	1284	39	8	8	7–57	15(17)	4.38	4.38	379	0.01	0.00(0)	9.22	0.17
D2#3	S3#3	200	99.8	2568	39	5	5	5–8	6(4)	0.60	0.60	734	0.00	0.04(0)	24.1	0.47
D16#3	S6#3	200	100	2568	39	27	13	8–39	17(7)	4.18	4.18	385	0.00	0.02(0)	24.1	0.47
D18#3	S13#3	200	100	2568	39	2042	6	6–28	7(2)	231	231	101	0.01	0.01(0)	24.1	0.47
D5#3	S5#3	200	50	3840	39	270	13	7–31	16(6)	25.1	25.1	212	0.01	0.01(0)	51.0	1.48
D8#3	S8#3	200	25	4488	39	4029	9	7–59	16(7)	3183	3220	42	1.15	3.87(1.1)	72.5	3.47
D24#3	S13#3	200	25	4488	39	91765	12	8–135	18(9)	9016	9549	29	5.59	9.65(0.3)	72.5	3.47

Notes: P_{in} (initial pressure) = pressure at the beginning of decompression ramp; P_f (final pressure) = pressure at which the experiment was quenched; t_{ramp} = duration of the ramp; $\|dP/dt\|$ = decompression/ascent rate [= $10^6(P_{in} - P_f)/(g d t_{ramp})$], with g = 9.81 m/s^2 and d = 2650 kg/m^3 (d = average density of crustal rocks); nd = not determined. X-ray microtomographic data acquired on entire charges (except V^d). n = number of bubbles counted in the analyzed volume. peak size = main peak diameter in bubble size distribution histograms. Range = total range of bubble size diameters. D = average bubble diameter. $V_{Equi.H_2O}$ and $V_{Equi.CO_2}$ = equilibrium vesicularities computed for the PST-9 composition considering the degassing of pure H$_2$O and pure CO$_2$, respectively (see text for details).
^{a} BND = bubble number density expressed in number of bubbles per mm^3 of the total sample (glass + bubbles).
^{b} BND$_{melt}$ = bubble number density per melt volume (without bubbles, following Proussevitch et al. 2007). S = average spacing between bubbles calculated from BND$_{melt}$ [$S = (3/4\pi BND_{melt})^{1/3}$; Lyakhovsky et al. 1996; Baker et al. 2006].
^{c} V = vesicularity (volume fraction of bubbles, vol%) measured from the total sample.
^{d} V = vesicularity measured from representative sub-volumes.
^{e} Textural data on the first bubble population of D24#1 charge.
^{f} Textural data on the second bubble population of D24#1 charge.
^{g} Standard deviation.

which are conditions known to be above the PST-9 liquidus on the basis of previous phase-equilibrium experiments (Di Carlo et al. 2006; Pichavant et al. 2009). Up to four capsules (one for each series plus the sensor capsule) were placed together in the IHPV for duration of about 40 h. According to H$_2$O and CO$_2$ melt diffusion calculations (Zhang and Ni 2010), initial experiments have shown that such a duration is sufficient to attain an equilibrium distribution of dissolved H$_2$O and CO$_2$ in the 2.5 mm diameter melt cores (Le Gall and Pichavant 2016). For the 5 mm diameter melt core, a run duration of 24 h was long enough to dissolve water and attain an equilibrium distribution. The synthesized crystal- and bubble-free glasses were used as starting materials in the decompression experiments (Table 3).

Each decompression run included up to three capsules (one for each series, Table 3). The experiments were conducted at a constant temperature of 1200 °C, from an initial pressure (P_{in}) of 200 MPa to final pressures (P_f) ranging between 200 (no decompression) and 25 MPa. The 5 mm diameter glass cylinder was decompressed to 60 MPa P_f. All runs began with a step of approximately 1 h at 200 MPa and 1200 °C, to re-equilibrate the starting volatile-bearing glasses. Pressure was then released manually to P_f at a decompression rate of 39 kPa/s (or 1.5 m/s taking a rock density of 2650 kg/m^3), which leads to decompression durations of 20–75 min depending on P_f. Immediately after attainment of P_f, decompression charges were rapid-quenched (within ~1–2 s) to freeze the glass textures and chemistries.

After the quench, capsules were weighted to check for leaks and then opened.

ANALYTICAL METHODS

Sample preparation

After each synthesis experiment, a part of the glass cylinder (one for each series) was analyzed by IR spectroscopy to check for the homogeneity of H$_2$O and CO$_2$ concentrations and distributions. To do so, sections were cut perpendicularly to the long axis of the glass cylinders, double-polished, and analyzed.

After the decompression experiments, the glass cylinders were carefully removed from their capsules. Their texture was studied by X-ray microtomography (the analysis is performed on the entire charge). Then, the glasses were subdivided into several sections, again cut perpendicularly to the cylinder long axis. One of these sections (or several sections when numerous analyses were needed) was double-polished for the determination of volatile concentrations dissolved in the glass, by IR spectroscopy. Another section was embedded into epoxy resin and polished for scanning electron microscope (SEM) observations.

The metallic pellets in the sensor capsule were also recovered, mounted in epoxy resin, and then analyzed by electron microprobe.

Textural analyses

We used the Phoenix Nanotom 180 at ISTO, Orléans, to perform X-ray computed tomography (X-ray CT) analyses of each post-decompression charge. Between 1000 and 1100 projection images were collected from the 360° rotation of the samples, using a tungsten filament and either a molybdenum (most of the time) or a tungsten (more rarely) target. During the acquisition of the X-ray CT scans, the glass cylinders were mounted on carbon fiber rods with thermoplastic adhesive. Operating voltages ranged from 90 to 110 kV, with filament currents of 58–170 µA. Voxel edge lengths ranged between 2.78 and 6.77 µm, and they represent the minimum bubble sizes that can be detected. Reconstruction of the projections into a stack of grayscale images was performed with a Phoenix program (datos|x reconstruction). Then, a complete three-dimensional reconstruction of the sample was produced using the ImageJ software package (Abràmoff et al. 2004). This allows the determination of the textural parameters [individual bubble volume, individual bubble size (D) calculated from volume assuming a spherical shape, bubble number density (BND) defined as the number of bubbles per unit volume of melt, average spacing between bubbles (S) and vesicularity (V), see Table 3],

following the procedure described in Le Gall and Pichavant (2016). Image analysis was performed either on entire X-ray CT data set (V^c determination, Table 3) or on four representative sub-volumes of each sample (V^d determination, Table 3). For charge D24#1 (Fig. 1c), the population of very large interconnected voids opened toward the exterior of the charge were counted as bubbles. Their sizes and number densities were estimated from two-dimensional tomographic slices.

For comparison with the vesicularities measured in our run products, theoretical vesicularities generated from equilibrium degassing were computed for the PST-9 melt composition, as detailed in Le Gall and Pichavant (2016). Two end-member cases were considered corresponding to the equilibrium degassing of pure H_2O and pure CO_2 gas, respectively.

A limited number of samples was examined by scanning electron microscopy (SEM), to check for the presence of bubbles that cannot be detected by X-ray CT because of their size (<4 μm). SEM images were collected using the MIRA3 TESCAN FEG instrument at ISTO, Orléans. An accelerating voltage of 15–25 kV was applied.

Glass volatile concentrations

H_2O and CO_2 contents in the samples were determined by Fourier transform infrared spectroscopy (FTIR). We used a Nicolet 6700 spectrometer and a Continuμm FTIR microscope, together with an IR source, a KBr beamsplitter, and a MCT/A

FIGURE 1. Representative types of textures of post-decompression glass samples. (**a**) Tomographic slice of sample D3#1 quenched at $P_f = P_{in} = 200$ MPa, showing a bubble-free core and a thin (<50 μm) bubbly rim indicated by black arrows. (**b**) Tomographic slice of sample D24#3 decompressed to 25 MPa P_f, showing three distinct zones: (1) a thick (150–200 μm) bubbly rim indicated by a black arrow, (2) a bubble-free zone depleted in volatiles delimited by a double black arrow, and (3) a core with numerous nearly homogeneously distributed bubbles. (**c**) Tomographic slice of sample D24#1 decompressed to 25 MPa P_f, characterized by two distinct bubble populations. The inset gives a close-up view of the small bubbles that correspond to the second bubble population. See Table 3 for details about the experimental conditions and textural results.

detector (mercury, cadmium, tellurium). Punctual analyses and concentration profiles, to control the homogeneity of the starting glass cores and the distribution of the volatiles, were performed with a 50 μm diameter spot. FTIR spectra were acquired between 650 and 7000 cm^{-1} on doubly polished samples (18–207 μm) from 128 scans collected at a resolution of 4 cm^{-1}. H_2O and CO_2 concentrations (C, wt%) were calculated from the Beer-Lambert law, as (e.g., Métrich et al. 2004):

$$C = \frac{100 \cdot A \cdot M}{\varepsilon \cdot \rho \cdot e} \tag{1}$$

where A is the absorbance (measured at 3530 cm^{-1} for H_2O and at 1515 cm^{-1} for CO_2), M the molar mass of the species (g/mol), ε the molar absorptivity [L/(mol·cm)], ρ the glass density (g/cm^3), and e the sample thickness (cm) measured with an optical microscope.

Absorbance of the 3530 cm^{-1} total H_2O band was measured with a straight base line, and that of the 1515 cm^{-1} carbonate ions band was determined by subtracting a spectrum obtained on a glass with no dissolved volatiles. For H_2O we considered a ε of 64 L/(mol·cm) (Dixon et al. 1995) and for CO_2, we calculated a ε of 363 L/(mol·cm) from the equation of Dixon and Pan (1995), as $\varepsilon^{1525} = 451-342$ [Na/(Ca+Na)]. Densities of the experimental glasses were calculated using the method of Richet et al. (2000), using the measured density of the anhydrous starting glass (ρ = 2.747 ± 0.001). With this method we consider only the amount of water dissolved in the glass and assume that the quantity of CO_2 dissolved does not significantly affect densities (Lange 1994; Bourgue and Richet 2001; Lesne et al. 2011a). Analytical uncertainties on volatile concentrations in glasses are ±0.1 wt% (H_2O) and ±100 ppm (CO_2).

Equilibrium gas-melt computations (volatile solubilities as a function of P-T conditions, isobaric solubility curves, and closed-system degassing paths) were calculated with the VolatileCalc model of Newman and Lowenstern (2002), for a basalt with 49 wt% SiO_2. H_2O and CO_2 contents in glasses from the synthesis experiments and from the series #1 decompression experiments were also compared with the recent experimental solubilities of Lesne et al. (2011a, 2011b) and Shishkina et al. (2010), determined for a pressure of 200 MPa and temperatures of 1200–1250 °C.

Electron microprobe analyses of metallic sensor phases were performed with the Cameca SX-50 at Orléans. Analyses were carried out under an acceleration voltage of 20 kV, counting times of 10 s, and a sample current of 20 nA.

EXPERIMENTAL RESULTS

Redox conditions

The mole fraction of Ni in the alloy phase of the sensor capsule (X_{Ni}) indicated a f_{H_2} of 9 bar. This translates to f_{O_2} conditions in the synthesis experiments ranging from NNO–1.4 (series #3) to NNO+0.1 (series #2) to NNO+0.9 (series #1) depending on the H_2O concentrations (and thus the f_{H_2O}) in the three experimental series (NNO is the f_{O_2} of the Ni-NiO equilibrium at the P-T of interest). The f_{O_2} conditions determined for series #1 and #2 melts are close to the f_{O_2} around NNO+0.5 determined for the near-liquidus evolution of "golden" pumice melts (Di Carlo et al. 2006). It is worth noting that the f_{O_2} determined for series #3 melts is more reduced, because of the lower melt H_2O concentrations (and so lower f_{H_2O}) measured in this series (see below).

H_2O and CO_2 concentrations in starting glasses

The volatile contents of the crystal- and bubble-free glasses from the synthesis experiments (hereafter designated as pre-decompression glasses) are presented in Table 2. No concentration gradients of either H_2O or CO_2 were observed on FTIR profiles from capsule walls toward glass cores. If the standard deviations and analytical errors for the volatile concentration measurements are considered, the pre-decompression glasses have homogeneous H_2O and CO_2 concentrations.

Starting glasses divide into three compositional groups according to the synthesis conditions (Table 2). Series #1 glasses contain about 4.92 ± 0.02 wt% dissolved H_2O and no CO_2.
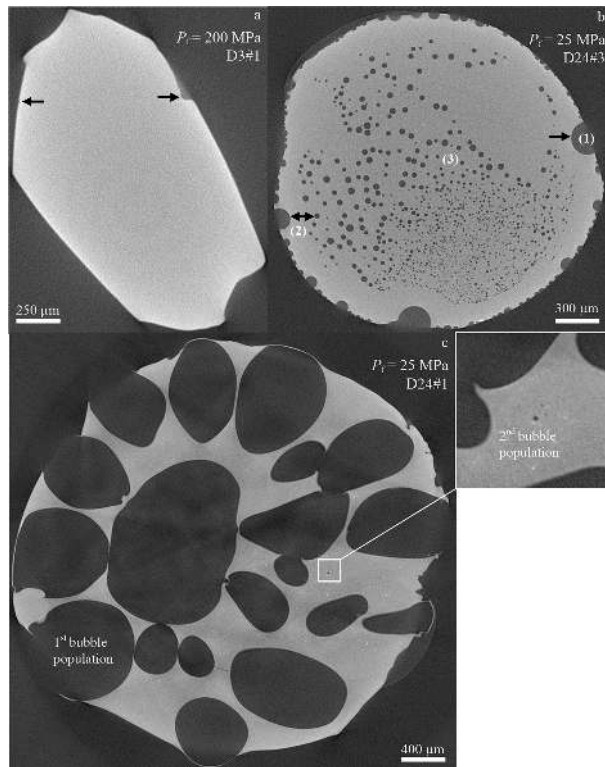
Water-saturated conditions were confirmed in series #1 charges by the presence of water bubbles hissing out from the capsules during their opening (Lesne et al. 2011b). The H_2O concentration measured in sample S8#1 is clearly lower (2.53 ± 0.05 wt%, Table 2) and thus appears anomalous, being excluded from the average. Actually, H_2O loss occurred in this charge during the experiment. Series #2 glasses have between 1.95 and 2.37 wt% H_2O and from 818 to 1011 ppm CO_2 (Table 2). One synthesis charge has a clearly lower H_2O content (0.58 wt%, S4#2) than the others. This deviation is related to an analytical problem (in spite of multiple checks, the analytical problem persisted). The glass decompressed from S4#2 to $P_f = P_{in} = 200$ MPa (D3#2 charge) was found to contain a reasonable H_2O concentration (2.45 wt%, Tables 3 and 5[1]). Therefore, the H_2O content of charge S4#2 is estimated to be around 2.5 wt%. Apart from S4#2, the series #2 volatile concentrations are within the range of melt inclusions in Stromboli "golden" pumices (H_2O = 1.8–3.4 wt%, CO_2 = 894–1689 ppm; Métrich et al. 2001, 2010; Bertagnini et al. 2003). Although water was not initially added in series #3 capsules ($X_{H_2O in}$ = 0, Table 2), this volatile component was found dissolved in all series #3 pre-decompression glasses (concentration range: 0.71–1.12 wt%, Table 2). Glass CO_2 concentrations are of the order of 850–1100 ppm. H_2O is generated through the reduction of the Fe^{3+} of the melt during synthesis, because of the pressurization of the vessel with H_2. The reduction reaction can be written (e.g., Lesne et al. 2011a):

$$Fe_2O_{3(melt)} + H_{2(vap/melt)} = 2FeO_{(melt)} + H_2O_{(melt)}. \qquad (2)$$

Part of the water may also come from the silver oxalate used as the CO_2 source, as mentioned by Lesne et al. (2011a), reaction (Eq. 2) being insufficient to account for the measured H_2O contents of series #3 glasses.

The dissolved H_2O and CO_2 concentrations in all compositional series are in agreement with the experimental solubilities found in basaltic melts equilibrated at 200 MPa, 1200–1250 °C (Shishkina et al. 2010; Lesne et al. 2011a, 2011b).

---

[1]Deposit item AM-16-95639, Table 5. Deposit items are free to all readers and found on the MSA web site, via the specific issue's Table of Contents (go to http://www.minsocam.org/MSA/AmMin/TOC/).

Textures of post-decompression glasses: Qualitative observations

Charges from the decompression experiments (hereafter designated as post-decompression glasses) were generally recovered as glassy blocks. Exceptions are provided by the series #1 charges decompressed to 25 MPa, which yielded a range of textures totally different from all the other charges from this paper. Bubbly glass fragments, foams (Fig. 1c), and in one case a glass powder were observed in the five series #1 charges decompressed to 25 MPa P_f (Table 4). All post-decompression glasses were crystal free. The absence of crystals was checked by optical microscopy on the doubly polished sections prepared for FTIR and also by SEM. Tiny oxide crystals (Ti-bearing magnetite, Di Carlo et al. 2006; Pichavant et al. 2009, 2013) occur in some charges but always in very small amounts. Some charges show evidence for bubble nucleation on those Fe-Ti oxides (Le Gall 2015). However, this was observed only for a negligible proportion of nucleated bubbles (i.e., for less than 1.5% of total bubbles in most charges and up to 6% in charge D5#2).

Two main types of post-decompression glasses were distinguished on the basis of textures observed in the core of the samples. The *first* type corresponds to bubble-free glasses (Fig. 1a). It concerns the D3#1 and D3#3 samples (Table 3). Although the interior of these glasses is completely devoid of bubbles, D3#1 charge exhibits a thin (<50 μm, Fig. 1a) bubbly rim resulting from heterogeneous nucleation on the inner wall of the capsule (e.g., Mourtada-Bonnefoi and Laporte 2002). The *second* type of post-decompression glasses is characterized by a nucleated core with a nearly homogeneous texture (Fig. 1b). Three distinct zones can be identified in these glasses: (1) a bubbly rim (generally up to ~300 μm, e.g., in the order of 150–200 μm in D24#3 sample, Fig. 1b) at the glass-capsule interface, followed by (2) a bubbly free zone (depleted in volatiles), and (3) a core with uniformly spaced bubbles having variable sizes, from a few micrometers up to 266 μm (range of bubble diameters, Table 3). Given the almost uniform spatial distribution of bubbles and the absence of crystals (hence of possible nucleation sites), we interpret the textures of type 2 post-decompression glasses to result from homogeneous bubble nucleation. Charge D1#2 is characterized by a somewhat heterogeneous distribution of relatively large bubbles (6–60 μm, Table 3). However, SEM imaging revealed the presence of a large

TABLE 4. Experimental details and textural data for the 25 MPa series #1 charges

Charge	PST-9 starting material	Capsule length (cm)	Capsule after experiment	Glass after experiment	Bubble texture	Interpretation capsule	Interpretation charge	Bubbles (vol%)
D12#1	Cylinder	3.5	Swollen around sample, weight gain, perforated around sample	Large blocks inside and outside the capsule	Bubbles (<2 to >100 μm)	Sample causes capsule failure	Coarsely fragmented	nd
D19#1	Cylinder	4	Unswollen, no weight change, unperforated	Glass powder inside the capsule	Bubbles (<4 to >200 μm)	No capsule failure	Finely fragmented	nd
D24#1	Cylinder	4	Entirely swollen, weight gain, perforated around sample	Foam leaked outside the capsule (3–4 mm diameter)	Highly vesicular	Sample causes capsule failure	Unfragmented	71.2
D27#1	Cylinder	5	Unswollen, weight?, perforated around sample	Dense block flown outside the capsule	Bubbles (<11 to 46 μm)	Sample causes capsule failure	Unfragmented	0.00
S+D40#1	Powder	4.5	Swollen around sample, weight gain	Foam and powder inside the capsule	Highly vesicular, slug	Sample causes capsule failure	Partially fragmented	High

Note: Experimental conditions: T = 1200 °C; P_{in} = 200 MPa; P_f = 25 MPa; t_{ramp} = 4488 s; $|dP/dt|$ = 39 kPa/s; nd = not determined.

population of smaller (<5 μm) bubbles, homogeneously distributed within the charge. This seems to be the case for charges D1#3 and D2#3, although no check for the presence of small bubbles could be performed by SEM because no samples were left for analysis.

Bubbles are absent in series #1 and #3 experiments quenched at $P_f = P_{in} = P_{synthesis} = 200$ MPa. In series #2, by contrast, the sample quenched at $P_f = 200$ MPa (D3#2) contains a few large bubbles (10 bubbles with an average size of 40 μm, Table 3). The presence of these bubbles may reflect an excess of the fluid phase (early excess fluid-phase bubbles), as observed by Lensky et al. (2006), or may correspond to trapped air bubbles. Consequently, these bubbles are not considered below as products of homogeneous nucleation.

Textures of post-decompression glasses: Quantitative observations

Textural information about the decompression experiments are given in Tables 3 and 4 and depicted in Figures 2–4.

Vesicularities range from 0 to 71.2 vol% (series #1), 0.01 to 13.8 vol% (series #2), and 0 to 9.25 vol% (series #3). It is worth noting that the series #1 charge (D24#1) with a 71.2 vol% vesicularity is part of the texturally specific 25 MPa P_f charges (Table 4). This charge yielded a highly vesicular foam that was found extruded out of the capsule (Fig. 1c). However, this unusual texture is not the result of capsule failure as detailed below, and is considered to be representative of the degassing process between 50 to 25 MPa P_f in series #1 charges. Consequently, the data from charge D24#1 will be given below full consideration. Another series #1 charge (D8#1) is also worth being detailed because it was performed with a pre-decompression melt having a H_2O concentration ~50% lower than all the other series #1 charges. D8#1 was decompressed to 25 MPa P_f and yielded a vesicularity of 1.45 vol% that cannot be directly compared with the data for the other series #1 charges. For this reason, D8#1 is plotted with a different symbol on Figure 2.

In general, vesicularity increases with decreasing P_f from 200 to 25 MPa (Fig. 2a, Tables 3 and 4), especially between $P_f = 50$ and 25 MPa. Besides the dependence on P_f, vesicularities are a function of the volatile series since the highest vesicularities are for the H_2O-rich glasses (series #1). For example, when decreasing the melt H_2O content at constant P_f (25 MPa, Fig. 2a), V decreases from 71.2 (series #1) to 13.8 (series #2) to 9.7 (series #3) vol%. Vesicularities for series #1 are lower than theoretical vesicularities calculated from equilibrium degassing, except the point at 25 MPa P_f that plots on the theoretical curve. The series #2 data plot intermediate between the two theoretical vesicularity curves, whereas the series #3 glasses plot close to the theoretical curve for CO_2 degassing (Fig. 2a).

Average bubble diameters in series #1 range from 8 to 741 μm. Charge D24#1 ($P_f = 25$ MPa, Fig. 1c) is characterized by two distinct bubble populations with sizes ranging from 9 μm to 1.8 mm. The first population has an average bubble size of 741 μm and the second of 17 μm (Fig. 2b). The series #1 D24#1 charge is the only one hosting a bubble population (the first one) with shapes that deviate significantly from spherical. In comparison with the other series #1 glasses, sample D8#1 ($P_f = 25$ MPa) deviates from the general behavior since bubble sizes are lower on average (28 μm) as a result of its lower pre-decompression melt H_2O concentration. For the series #2 samples, D ranges from 13–74 and

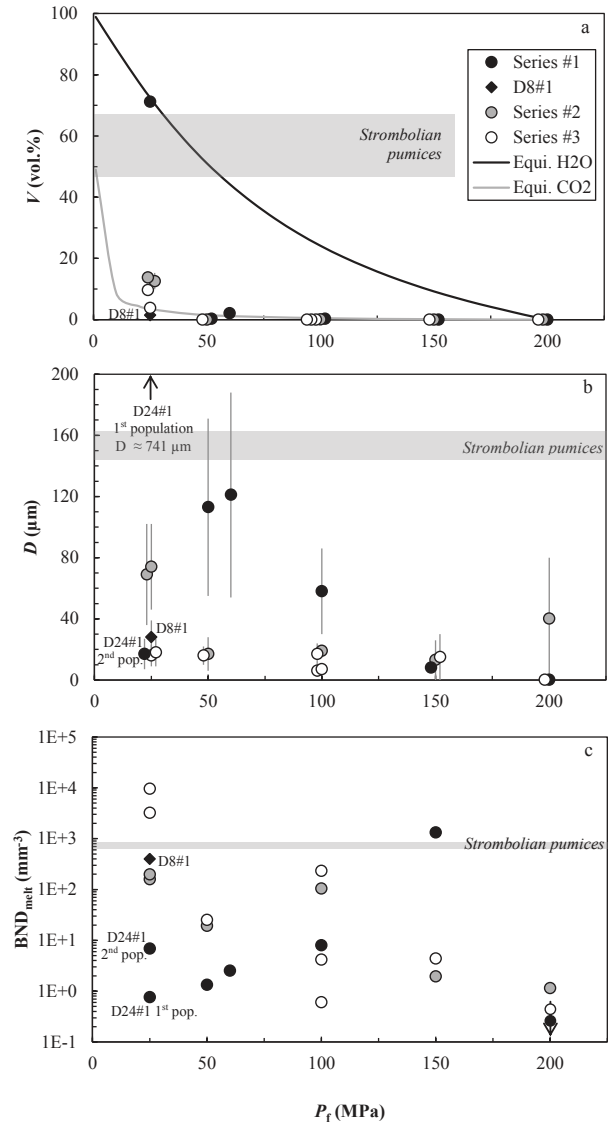**FIGURE 2.** (**a**) Vesicularity V, (**b**) average bubble diameter D, and (**c**) bubble number density per unit volume of melt BND$_{melt}$ plotted as a function of final pressure P_f for the post-decompression glasses of this study. Experimental data in Table 3. The three glass series are distinguished, series #1 = black circles; series #2 = gray circles; series #3 = white circles. The series #1 charge D8#1 is plotted with a different symbol (black diamond) since it started from a pre-decompression melt with a H_2O concentration ~50% lower than all the other series #1 charges. In **a**, equilibrium vesicularities (thick black and gray lines) calculated for pure H_2O and CO_2 degassing, respectively (see text), are shown for comparison with the experimental data. Both the first and the second bubble populations of sample D24#1 (Table 3) are plotted in **b** and **c**. In **a** and **b**, error bars (standard deviations, Table 3) are indicated on the data points. The V, D, and BND$_{melt}$ values for Strombolian pumices (data from Polacci et al. 2006, 2009) are shown for comparison with the experimental data points.

6–18 μm for the series #3. For the three series, bubble diameter generally increases with decreasing P_f from 200 to 25 MPa (Fig. 2b, Table 3). The average bubble diameter is also dependent on
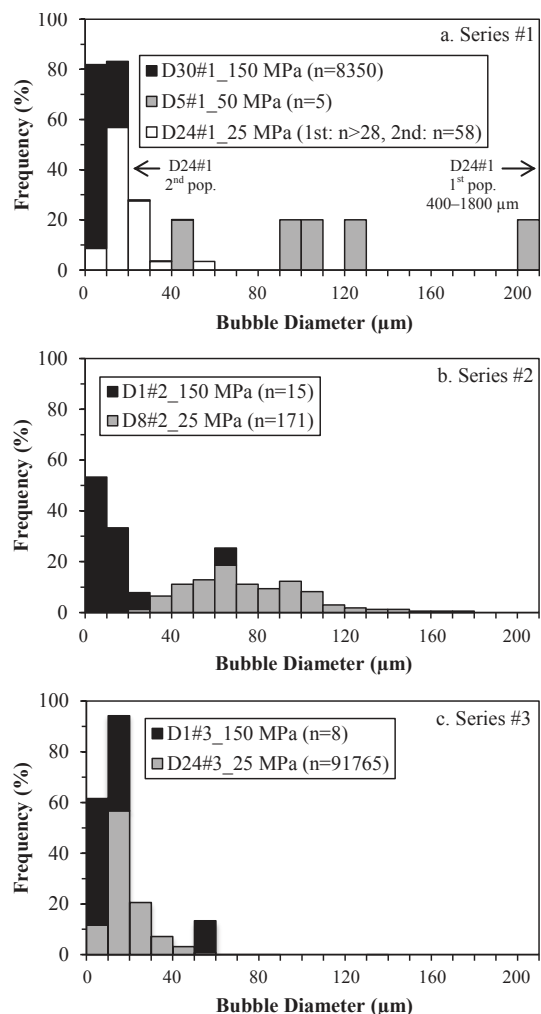
FIGURE 3. Evolution of the bubble size distribution (BSD) during decompression within each glass series. (**a**) Series #1, (**b**) series #2, (**c**) series #3 post-decompression glasses. For each glass series, two post-decompression glass samples are detailed, one representative of the early and the other of the late stage of the nucleation process. Note that for series #1 glasses, the D24#1 charge is also detailed. For each post-decompression glass sample, histograms show frequencies (normalized to 100%) of diameters of individual bubbles in the population (or the two populations for charge D24#1) using size classes of 10 μm each. The range of bubble diameters of each population is given in Table 3. The number of bubbles within each population is specified (n, Table 3). Details about experimental conditions and other textural data in Table 3.

the concentration of dissolved volatiles. The larger bubble sizes are for the H_2O-rich series #1 post-decompression glasses (741 μm at 25 MPa P_f), decreasing with lowering the melt H_2O content (69–74 μm for series #2 and 16–18 μm for series #3).

Bubble number densities (BND_{melt}, Table 3 and Fig. 2c) range from about 10^0 to 10^2 mm⁻³ (series #2), 10^3 mm⁻³ (series #1), and 10^4 mm⁻³ (series #3). Upon decreasing P_f, BNDs of series #1 glasses generally decrease, from 10^3 mm⁻³ (150 MPa, D30#1) to 10^0 mm⁻³ (50 MPa, D5#1). Nevertheless, two BND increases are observed along the decompression path, the first and largest between 200 (0 mm⁻³, D3#1) and 150 MPa and the second from

50 to 25 MPa (10^0–10^1 mm⁻³, D24#1) . In contrast, the series #2 and #3 glasses have BNDs generally increasing from 200 (10^0 and 0 mm⁻³, D3#2 and D3#3) to 25 MPa (10^2 and 10^4 mm⁻³, D8#2 and D24#3) . Nevertheless, in both glass series there are a few exceptions characterized by BND decreases, for example between P_f = 150 and 100 MPa for one series #3 charge and between P_f = 100 and 50 MPa for one series #2 and also one series #3 charge (Fig. 2c).

Bubble size distributions (BSDs) are analyzed from histograms based on the diameter of the bubbles (Fig. 3) and from cumulative distributions of volumetric classes (Fig. 4), constructed for each series. Two main types of distributions were distinguished in Figure 4, exponential and power law, although the two are mixed in most samples. Regressions were performed with Excel software. Very good fits were generally obtained, yielding $R^2 > 0.99$ for more than 50% charges. Series #1 glasses are initially (at P_f = 150 MPa) characterized by bubbles sizes ranging between 4 and 46 μm (D30#1, Fig. 3a, Table 3), leading to a power law bubble size distribution with an exponent of 1.91 (Fig. 4a). Then, from P_f = 100 to 50 MPa bubbles become larger (40–200 μm, D5#1) and multiple peaks occur in the histogram (Fig. 3a), corresponding to exponential distributions (Fig. 4a). It is worth mentioning that the bubble size distribution in D5#1 is uncertain because of its low number of bubbles. At P_f = 25 MPa, the two bubble populations in D24#1 charge have sizes of 400–1800 and 9–56 μm, respectively (Fig. 3a). The former exhibits a power law and the latter a mixed power law–exponential distribution with exponents of 0.50 and 0.63, respectively (Fig. 4a). Series #2 glasses have bubble sizes from 6–60 μm at 150 MPa P_f (D1#2, Fig. 3b, Table 3) to 15–48 μm at 100 MPa (D2#2, Table 3), both fitted by power law distributions with exponents of 0.49 and 2.22, respectively (Fig. 4b). Upon decreasing P_f, bubble sizes become larger (24–175 μm, D8#2, P_f = 25 MPa, Fig. 3b and Table 3), yielding mixed power law–exponential distributions (Fig. 4b). In fact, two types of distributions can be recognized in the charges decompressed to P_f = 50 and 25 MPa: the small- to medium-sized bubbles can be fitted by an exponential function, whereas the larger bubbles are best described by a power law with an exponent of 0.78–1.96. Series #3 post-decompression glasses have numerous small bubbles (<10 μm, Fig. 3c) at 150 MPa P_f (range: 7–57 μm, D1#3, Table 3). Upon lowering P_f to 25 MPa, the bubbles become a little larger (8–135 μm, D24#3, Table 3), and the maximum is shifted to 10–20 μm (Fig. 3c). The BSDs are characterized by both power law and exponential shapes (Fig. 4c). For example, glasses decompressed to P_f = 150 and 50 MPa (D1#3 and D5#3, Fig. 4c) are best described by exponential functions, while the three duplicated glasses decompressed to 100 MPa P_f can be described by either power law functions (D2#3 and D18#3, Fig. 4c) or a combination of both (D16#3, Fig. 4c) as the two samples decompressed to 25 MPa P_f (D8#3 and D24#3, Fig. 4c). It is worth noting that two charges with exponential distributions yielded relatively poor fits (Fig. 4c): D1#3 (P_f = 150 MPa, R^2 = 0.88) and D24#3 (P_f = 25 MPa, R^2 = 0.94 for the small-to-medium bubble sizes).

H_2O and CO_2 concentrations in post-decompression glasses

H_2O and CO_2 concentrations in post-decompression glasses are presented in Table 5[1] and shown in Figure 5. Series #1 glasses
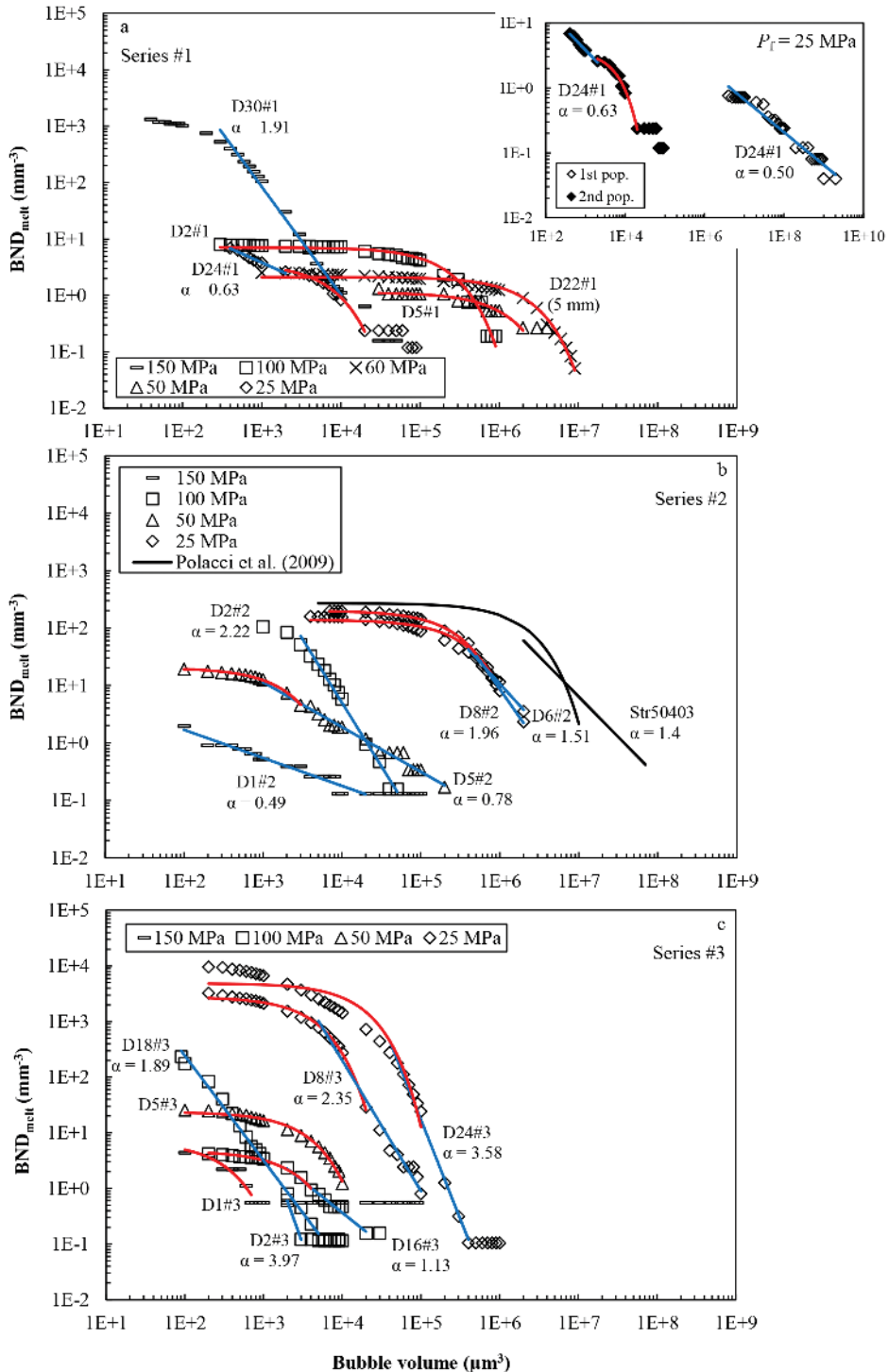
FIGURE 4. Bubble size distributions (BSD) expressed as log-log plots of bubble number density (BND_{melt}, in mm^{-3}) vs. bubble volume for all post-decompression glasses from this study. For each glass sample, the bubble population is characterized by a range of bubble size (expressed as diameters in Table 3) and a bubble number density value (Table 3). Each point along the distribution curve corresponds to the number of bubbles with a volume strictly larger than indicated. (**a**) Series #1 glasses, (**b**) series #2 glasses, and (**c**) series #3 glasses. Rectangles = glasses decompressed to 150 MPa P_f (final pressure); triangles = glasses decompressed to 100 MPa P_f; crosses = glass decompressed to 60 MPa P_f; squares = glasses decompressed to 50 MPa P_f; diamonds = glasses decompressed to 25 MPa P_f. The inset in **a** shows the bubble size distributions of the two bubble populations in charge D24#1. The blue continuous lines are power law fits and the red continuous curves are exponential fits, both regressed with Excel software. α is the power law exponent. The bubble volume distribution (black continuous line and curve) of a pumice sample from Polacci et al. (2009, Str50403 from a paroxysmal explosion at Stromboli) is given in **b** for comparison with the experimental BSDs. (Color online.)

have H_2O contents ranging from 4.91 wt% (D3#1, $P_f = 200$ MPa) to 1.52 wt% (D8#1, $P_f = 25$ MPa). Thus, a general decrease of the concentration of dissolved H_2O is observed when decreasing P_f (Fig. 5a). Considering the analytical uncertainties (Fig. 5a, Table 5[1]), the H_2O contents of series #1 glasses are in good agreement with H_2O solubilities determined by Lesne et al. (2011b), with the exception of two glasses decompressed to $P_f = 60$ (D22#1) and 50 (D5#1) MPa that have H_2O concentrations slightly exceeding solubilities (H_2O supersaturations of 0.2–0.35 and 0.3 wt% absolute for D22#1 and D5#1, respectively, Fig. 6). In addition, in these two series #1 charges, H_2O concentrations are close to solubilities near the glass-capsule interface and become higher in the core of the glass cylinder (Fig. 6). The fact that the increase of the H_2O concentration toward the core is more progressive in the charge with the larger diameter (D22#1, 5 mm) is consistent with a mechanism of diffusive motion of H_2O inside the melt toward the gas phase.

Series #2 post-decompression glasses have H_2O concentrations ranging between 2.45 and 0.82 wt% and CO_2 concentrations ranging from 850 to 550 ppm (Table 5[1]). Both their H_2O and CO_2 contents progressively decrease with P_f (Fig. 5b). However, the drop in H_2O and CO_2 concentrations is nonlinear with P_f. For example, the glass decompressed to 50 MPa has a much lower H_2O content (0.82 wt%, D5#2) than the glasses decompressed to 25 MPa (1.60 wt%, D6#2 and D8#2), and a higher CO_2 content (775 ppm) than the two glasses decompressed to 150 (754 ppm, D1#2) and 100 MPa (732 ppm, D2#2). Degassing trajectories in our experiments are different from closed-system equilibrium decompression trends, in that there is a marked drop of H_2O content for a comparatively slight CO_2 decrease. All post-decompression glasses retain elevated CO_2 concentrations, since the data points plot well above their respective gas-melt saturation isobars. For example, measured CO_2 contents in the glasses decompressed to 25 MPa (550–558 ± 62–76 ppm, D6#2 and D8#2) largely exceed the calculated value (<50 ppm).

Series #3 glasses have H_2O contents ranging between 0.69 and 0.95 wt% and CO_2 contents ranging from 873 to 461 ppm (Table 5[1]). Post-decompression glass CO_2 concentrations progressively decrease from 873 (D1#3, $P_f = 150$ MPa), 699–540 (D2#3, D16#3, and D18#3, $P_f = 100$ MPa), 626 (D5#3, $P_f = 50$ MPa) to 513–461 ppm (D8#3 and D24#3, $P_f = 25$ MPa), at approximately constant melt H_2O contents (Table 5[1] and Fig. 5c). Taken globally, the data points follow degassing trajectories that are nearly vertical, as are the theoretical equilibrium closed-system decompression paths. However, the decompressed glasses retain CO_2 contents that are well above equilibrium values. For example, at $P_f = 25$ MPa the equilibrium CO_2 concentration is <100 ppm while our samples contain 461 ± 80 (D8#3) and 513 ± 94 ppm CO_2 (D24#3, Table 5[1]).

INTERPRETATION AND DISCUSSION OF EXPERIMENTAL OBSERVATIONS

Supersaturation pressures required for homogeneous bubble nucleation

The homogeneous nature of bubble nucleation in our experiments is supported by the lack of crystals to serve as nucleation sites in the melts, and by the near textural homogeneity of our post-decompression glasses, as shown by the quite homogeneous distribution of bubbles in the total volume of the samples. Additional supporting arguments include the little spatial variation of the bubble number density inside the glass and the small dispersion of bubble sizes in a given sample.

From our decompression experiments, we can determine the supersaturation pressure required to trigger homogeneous bubble nucleation ΔP_{HoN}, which is defined as the difference between the saturation pressure ($P_{sat} = P_{in}$, except in charge D8#1 considered apart) and the final pressure (P_f) at which bubbles begin to form homogeneously. In each post-decompression glass series, we observed a transition from a bubble-free glass core (except for series #2, where we noted the presence of heterogeneously nucleated bubbles at $P_f = 200$ MPa) at a high P_f to a nucleated glass core at a lower P_f. As previously mentioned, in series #1 post-decompression glasses, bubbles are absent at $P_f = 200$ MPa (D3#1, Table 3 and Fig. 1a). They appear uniformly distributed in the melts from $P_f = 150$ MPa (D30#1, Table 3), suggesting that homogeneous bubble nucleation takes place between 200 and 150 MPa P_f, hence a $\Delta P_{HoN} \leq 50$ MPa. The series #1 D8#1 sample made from a pre-decompression melt with a low H_2O concentration yields a ΔP_{HoN} of 40–45 MPa by taking a P_{sat} of 65–70 MPa (Lesne et al. 2011b). Overall a critical supersaturation pressure of 45 MPa maximum is determined for the series #1 melts. This ΔP_{HoN} value is consistent with that found by Le Gall and Pichavant ($\Delta P_{HoN} \ll 50$ MPa 2016) in their faster decompression rate experiments. This range of ΔP_{HoN} value is less than recorded for more evolved melts (60–150 MPa; Mangan and Sisson 2000, 2005; Mourtada-Bonnefoi and Laporte 2004; Iacono-Marziano et al. 2007; Gardner and Ketcham 2011), reinforcing the idea that bubble nucleation takes place at low supersaturations in hydrous basaltic melts (Le Gall and Pichavant 2016).

The series #2 melts contain a few heterogeneously nucleated bubbles at $P_f = 200$ MPa (D3#2, Table 3). At $P_f = 150$ MPa, the D1#2 glass contain small (main peak diameter of 6–7 μm) bubbles. Only 15 bubbles were detected by X-ray CT because their size is hardly higher than the instrumental spatial resolution. Yet, SEM imaging revealed the presence of a population of small (<6 μm) uniformly distributed bubbles, suggesting that an event of homogenous nucleation takes place between 200 and 150 MPa P_f. Therefore, a ΔP_{HoN} of 50 MPa maximum is inferred for the series #2 melts. This value is less than found for similar compositions in the study of Le Gall and Pichavant (2016, $\Delta P_{HoN} < 100$ MPa) performed at a faster decompression rate. Pichavant et al. (2013) found a supersaturation pressure of 150 MPa maximum in their experiments performed on compositions similar to our series #2 melts. However, no data were given for $P_f > 50$ MPa, and so it cannot be excluded that, in their decompression experiments, homogeneous bubble nucleation would start at pressures > 50 MPa, leading to $\Delta P_{HoN} \ll 150$ MPa.

Series #3 post-decompression glasses are bubble-free at $P_f = 200$ MPa (D3#3, Table 3). We observed small (main peak diameter of 8 μm) bubbles in the glass core decompressed to $P_f = 150$ MPa (D1#3, Table 3). The number of bubbles analyzed by X-ray CT is very small (8 bubbles) presumably because of their small size. However, they indicate an event of homogenous bubble nucleation between 200 and 150 MPa P_f. From this observation, a ΔP_{HoN} of 50 MPa maximum is also inferred
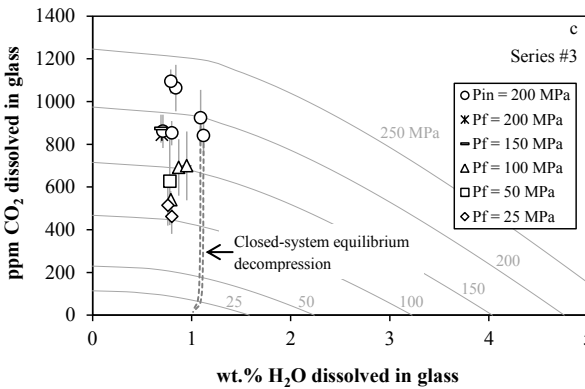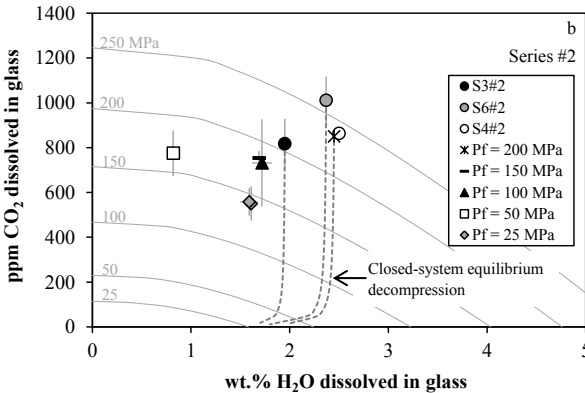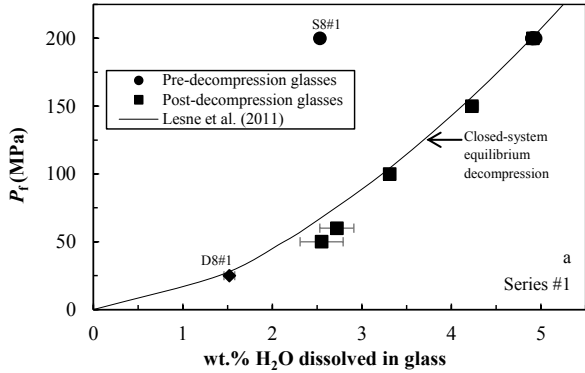
FIGURE 6. FTIR profiles of H_2O concentrations across the cylinder starting from the sample edge toward the core for series #1 glasses decompressed to different P_f from 150 to 25 MPa (note that the 25 MPa data points are for the D8#1 charge performed with a low H_2O concentration pre-decompression melt). The 150, 100, 50, and 25 MPa P_f cylinders have diameters ~2.5 mm; the 60 MPa P_f cylinder has a diameter of ~5 mm. Average H_2O concentration data are given in Table 5. H_2O solubilities (at pressures of 150–25 MPa, dashed horizontal lines) come from Lesne et al. (2011b).

FIGURE 5. H_2O and CO_2 concentrations in pre- and post-decompression glasses. (**a**) Plot of series #1 H_2O concentrations as a function of final pressure P_f. H_2O solubilities are computed using the Lesne et al. (2011b) regression equation. They define the closed-system equilibrium decompression path (black continuous line). H_2O vs. CO_2 concentrations in series #2 and #3 glasses are shown in **b** and **c**, respectively. Circles = pre-decompression glasses synthesized at 200 MPa P_{in} (initial pressure); crosses = glasses decompressed to 200 MPa P_f (final pressure); rectangles = glasses decompressed to 150 MPa P_f; triangles = glasses decompressed to 100 MPa P_f; squares = glasses decompressed to 50 MPa P_f; diamonds = glasses decompressed to 25 MPa P_f. In **b**, the symbol color refers to the synthesis experiments, either S3 (black), S6 (gray), or S4 (white, Table 2). Error bars (standard deviations, Table 5) are indicated on the data points. The thin continuous lines are fluid-melt equilibrium saturation isobars (25–250 MPa) and the dashed curves are equilibrium decompression paths calculated for some series #2 and #3 glasses assuming closed-system behavior. Equilibrium fluid-melt calculations were performed with VolatileCalc (Newman and Lowenstern 2002).
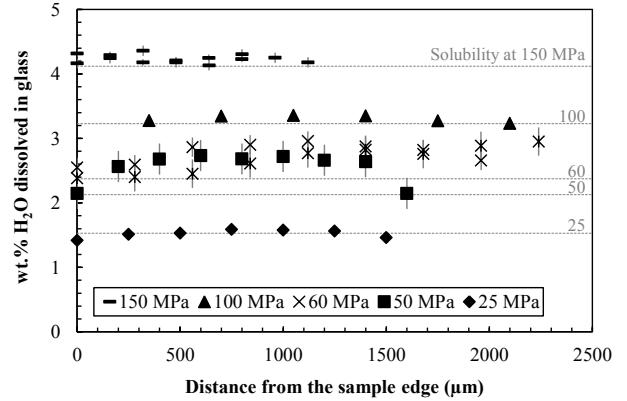
for the series #3 melts. This ΔP_{HoN} value is the same as found for similar compositions in the study of Le Gall and Pichavant (2016) performed at a faster decompression rate. For comparison, a critical supersaturation pressure of 200 ± 100 MPa was found by Lensky et al. (2006) for CO_2 bubbles in a synthetic mafic melt decompressed from 1.5 GPa, larger than determined here for series #2 and #3 melts. However, it is worth specifying that Lensky et al. (2006) worked on nominally H_2O-free melts. The range of supersaturations ($\Delta P_{HoN} \leq 50$ MPa) found in our series #2 and #3 melts is less than recorded for the nucleation of H_2O-CO_2 bubbles in more evolved melts (160–350 MPa, Mourtada-Bonnefoi and Laporte 2002).

Because the range of supersaturation pressures required for homogeneous nucleation is essentially the same ($\Delta P_{HoN} \leq 50$ MPa) for each glass series, it is difficult from our data to quantify the effects of H_2O and CO_2 on ΔP_{HoN}, as proposed for melts more evolved than basalts (Mourtada-Bonnefoi and Laporte 2002; Gardner and Webster 2016). In addition, our experimental results confirm previous observations and conclusions on the fact that ΔP_{HoN} values ≤ 50 MPa are specific to basaltic compositions, and that bubble nucleation takes place at low supersaturations in H_2O- and H_2O-CO_2-bearing basaltic melts (Le Gall and Pichavant 2016).

Surface tensions (σ) have been calculated (Appendix) by taking the supersaturation pressures determined for each series and our measured experimental nucleation rates. The supersaturation pressures are given as maxima, hence the calculated surface tensions are upper limits. Computations give maximum σ values ranging from 0.054 (series #1) to 0.059 N/m (series #2 and #3). For comparison, Le Gall and Pichavant (2016) obtained maximum surfaces tensions of 0.058 (series #1), 0.059 (series #3) and 0.091 (series #2) N/m for the same melt compositions and volatile concentrations. The differences observed (mostly for series #2 melts) are related to differences in supersaturation

pressures between the two studies since the decompression rate is not expected to have a significant influence on the bubble nucleation pressure (Mourtada-Bonnefoi and Laporte 2004). Note that the apparently large difference between supersaturation pressures in the two studies (series #2) is probably in part due to the large intervals between our experimental P_f. Le Gall and Pichavant (2016) observed bubbles homogeneously nucleated from 100 MPa (from 150 MPa in this study), but these could have started to form at pressures below than but close to 150 MPa. In the same way, Pichavant et al. (2013) found a σ of 0.18 N/m maximum for compositions as our series #2 melts. This maximum is higher than determined here, but again consistent with their higher supersaturation pressures ($\Delta P_{HoN} < 150$ MPa). Surface tensions from this study are lower than the values found by Khitarov et al. (1979): 0.1 to 0.4 N/m for basaltic melts at 1200 °C and 100–500 MPa, the lowest end of the range corresponding to hydrous compositions.

Physical mechanisms of degassing and textures

In this section, we discuss the physical mechanisms of degassing occurring in our decompression experiments, from nucleation, growth, and coalescence of gas bubbles, up to fragmentation. Emphasis is placed on textural differences between the three glass series.

Vesicularities. The three series of post-decompression glasses have vesicularities that generally increase upon decompression (i.e., upon decreasing P_f). The general increase in vesicularity observed upon decreasing P_f is consistent with a mechanism of progressive melt vesiculation associated with decompression. It is worth remembering that, for all glass series, the increase in vesicularity is the most strongly marked between $P_f = 50$ and 25 MPa (Fig. 2a). Nevertheless, the series #2 measured vesicularities are lower than expected for a closed-system degassing. It is also the case of the series #1 glasses decompressed up to 50 MPa P_f whose measured vesicularities remain very low (<3%), well below equilibrium values. It is recalled that the series #1, 25 MPa P_f D24#1 charge has a very high vesicularity (71.2%), slightly above the range of vesicularities for Strombolian pumices (47 and 67%, Polacci et al. 2006). Apart from that charge, our experimental vesicularities are systematically lower than equilibrium values. This is interpreted to result from the combination of two processes: (1) diffusive volatile loss from the melts and (2) bubble outgassing. On the one hand, diffusive volatile loss is demonstrated by the H_2O concentration profiles in the series #1, 60 and 50 MPa P_f samples (Fig. 6). Calculations of diffusion distances for H_2O and CO_2 using the diffusion coefficients from Zhang and Ni (2010) show that H_2O can migrate out of the sample over lengths <2 mm (for a duration of 4500 s that corresponds to the longest experiments), whereas the mobility of CO_2 is much lower. On the other hand, bubble outgassing would account for the reduction in BNDs observed in particular between 100 and 50 MPa (Fig. 2c). However, textures such as bubble accumulation on top of the charges, systematically elongated bubble shapes, and charges totally devoid of bubbles have generally not been observed. Calculations of the gravity-driven upward movement of the water bubbles have been performed using the Hadamard-Rybcynski bubble velocity equation (Bottinga and Javoy 1990). In detail, results depend sensitively on the bubble diameter, the

gas density, and the viscosity of the melt. For series #1 melts, calculated distances are ~2–3 mm for bubbles of 60 μm diameter (and ~9–14 mm for bubbles of 120 μm) and ascent durations of 21 min (corresponding to the 100–50 MPa P_f interval), suggesting that outgassing possibly takes place in our experiments and can contribute to the loss of the larger bubbles and the reduction in vesicularity.

Nucleation events. The melt vesiculation mechanism observed in our experiments results from different sub-processes that include bubble nucleation, growth, coalescence, and outgassing, as well as fragmentation. Textural evidence (bubble size distributions and bubble number densities) can be used to distinguish between single vs. multiple bubble nucleation events (or pulses) in our experiments. In series #1 post-decompression glasses, a large increase of BND is first observed from $P_f =$ 200 ($BND_{melt} = 0$ mm^{-3}) to 150 ($BND_{melt} = 1325$ mm^{-3}, Table 3, Fig. 2c) MPa, implying that an event of homogeneous bubble nucleation takes place. Then, there is a general decrease of BND with decreasing P_f from 150 to 50 ($BND_{melt} = 1.33$ mm^{-3}) MPa. This trend reflects a mechanism of bubble coalescence combined with bubble outgassing. This interpretation is supported by the small number (5) of bubbles in the charge decompressed to 50 MPa (D5#1) and the very low (<3%) vesicularities measured up to 50 MPa P_f. In addition, textural differences exist between the two charges of different diameter decompressed to $P_f = 60$ (D22#1) and 50 (D5#1) MPa. The 5 mm diameter charge (D22#1) contains many more bubbles (149), and accordingly has a higher vesicularity (2.1%) than the 2.5 mm diameter charge (5 bubbles and 0.3% vesicularity). This suggests that, with a higher diameter charge, diffusive H_2O loss and bubble outgassing from the melt are both limited. Although we do not observe BND stabilization (which would be marked by a horizontal line in Fig. 2c and would reflect the end of a nucleation event), the absence of small (<10 μm) newly formed bubbles from 100 to 50 MPa P_f testifies to the end of the first nucleation event. This is also suggested by the exponential distributions of bubble sizes from $P_f = 100$ to 50 MPa (Fig. 4a) that are indicative of an absence of small bubbles. Below 50 MPa, an additional increase of BND is observed, suggesting that a second nucleation event takes place between 50 and 25 MPa P_f. This is supported by the small newly formed bubbles in D24#1 as revealed both by X-ray CT and microscopic textural observations (second population with main peak diameter 10 μm, Fig. 1c). It is also worth emphasizing that the 4 other charges decompressed to 25 MPa P_f contain a population of small bubbles (Table 4). The mechanism of bubble nucleation observed in series #1 melts is thus discontinuous and restricted to two narrow P_f intervals (200–150 and 50–25 MPa).

In series #2 glasses, a general increase of the BND is observed from $P_f = 200$ ($BND_{melt} = 1.15$ mm^{-3}) to 100 ($BND_{melt} = 104$ mm^{-3}, Table 3, Fig. 2c) MPa that corresponds to the beginning of a homogeneous bubble nucleation mechanism. It is worth noting that the early event of heterogeneous bubble nucleation observed in charge D3#2 ($P_f = 200$ MPa) leads to a small number (10) of bubbles and, accordingly, to a low but nonzero BND. Below 100 MPa, we observe a decrease of BND ($BND_{melt} = 19.2$ mm^{-3}, D5#2, $P_f = 50$ MPa) that is interpreted to reflect a mechanism of bubble coalescence, and possibly bubble outgassing. As a result, the number of bubbles is reduced from

665 (D2#2, P_f = 100 MPa) to 114 (D5#2, P_f = 50 MPa). At the same time, bubble sizes give evidence for the appearance of small (<10 μm) newly formed bubbles, indicating the occurrence of secondary nucleation events. The evolution below 50 MPa and down to 25 MPa P_f is marked by an increase of the BND that is interpreted as the continuation of the same nucleation process.

In series #3 melts, an increase of BND is observed from P_f = 200 (BND_{melt} = 0 mm^{-3}) to 150 MPa (BND_{melt} = 4.38 mm^{-3}, Table 3, Fig. 2c) that corresponds to the beginning of a homogeneous bubble nucleation mechanism. Below 150 MPa, three cases were observed, either a continuous increase of the BND (D18#3), a decrease of the BND (D2#3) or a near-steady evolution of the BND (D16#3). The first case suggests the continuation of the same nucleation process below 150 MPa. This interpretation is supported by an increase in the number of bubbles from 8 (P_f = 150 MPa, D1#3) to 2042 (P_f = 100 MPa, D18#3), by the appearance of small (main peak size of 6 μm, Table 3) newly formed bubbles and by the power law distribution of the bubble sizes (Fig. 4c) that suggests that small bubbles are continuously appearing. The second case is interpreted to reflect a mechanism of bubble coalescence. However, numerous small (<5 μm) bubbles could not be measured in D2#3, and so its BND is underestimated. The third case corresponds to a BND stabilization that reflects the end of a nucleation event and the beginning of bubble growth and coalescence. In this sense, the BSD of charge D16#3 evolves to a mixed power law–exponential relation that indicates a decrease in the number of small newly formed bubbles and an increase in the number of larger bubbles (Fig. 4c). Below 100 MPa and down to 50 MPa P_f, two new situations are possible, either an increase of the BND (continuous bubble nucleation) or a decrease of the BND (bubble coalescence). In any case, the evolution below 50 MPa and down to 25 MPa P_f is marked by an increase of BNDs, which is interpreted as the continuation of the same nucleation process and the occurrence of secondary nucleation events.

We conclude to a major difference in the mechanism of bubble nucleation between series #1, on the one hand, and series #2 and #3, on the other hand, as observed in the experiments of Le Gall and Pichavant (2016). In H_2O-rich melts, two distinct events of bubble nucleation occur in narrow P_f intervals (the first at high pressure and the second at low pressure). In contrast, in CO_2-bearing melts, a single mechanism of continuous bubble nucleation takes place over a substantial P_f interval along the decompression path, leading to multiple bubble nucleation events.

Bubble coalescence. Textural evidence (decrease of the BND and common coalescence structures) can be used as indicators of bubble coalescence process in our experiments. Common coalescence structures were generally not observed in the three glass series. Therefore, evidence for coalescence mainly comes from decrease of BNDs and bubble numbers and possibly from the increase in bubble sizes. It is worth mentioning that a decrease of BND can also be due to bubble outgassing (see above). The series #1 post-decompression glasses are characterized by a general decrease of the BND from P_f = 150 to 50 MPa (Fig. 2c). This decrease is associated with a reduction in the number of bubbles from 8350 (D30#1, P_f = 150 MPa) to 5 (D5#1, P_f = 50 MPa) and with a large increase of the average bubble size (Fig. 2b), suggesting that both bubble growth and coalescence take place in

series #1 melts. In fact, a few coalescence structures (dimpling, Castro et al. 2012) were observed in the charge decompressed to P_f = 60 MPa (D22#1). In addition, the evolution of the bubble size distribution from power law to exponential indicates the presence of larger bubbles interpreted to result from coalescence (Figs. 3a and 4a). Therefore, as observed in the experiments of Le Gall and Pichavant (2016), bubble coalescence starts very early along the decompression path in series #1 glasses. It is worth mentioning that the charge decompressed to 25 MPa P_f (D24#1) present numerous coalescence structures (dimpling, bending, and stretching; Castro et al. 2012; Martel and Iacono-Marziano 2015; Le Gall and Pichavant 2016) involving particularly large (up to 1.8 mm) bubbles (Fig. 1c) whose shape deviates from spherical. This suggests that the mechanism of bubble coalescence continues below 50 MPa and until 25 MPa P_f.

In series #2 glasses, the decrease of BND observed between 100 and 50 MPa P_f (Fig. 2c) provides evidence for the occurrence of a bubble coalescence mechanism. In this way, the number of bubbles decreases from 665 (D2#2, P_f = 100 MPa) to 114 (D5#2, P_f = 50 MPa). Increases in the average and the main bubble sizes are, however, hidden by the superimposition of a bubble nucleation process that continuously generates small (<10 μm) bubbles and contributes to reduce bubble sizes.

In series #3 glasses, two decreases of BND are observed, the first between 150 and 100 MPa P_f and the second between 100 and 50 MPa P_f, both interpreted as evidence for coalescence. However, it is worth mentioning that the observed BND evolutions for the different charges at 100 and 50 MPa P_f indicate that coalescence is not systematic. We interpret these differences from one charge to the other at a given P_f to reflect variations in distances between bubbles. For example, the average distance between bubbles in charges D2#3 (734 μm) and D16#3 (385 μm) is larger than in charge D18#3 (101 μm), all at P_f = 100 MPa. This would make bubble interactions upon further decompression progressively more difficult in charges such as D2#3 and D16#3 than in D18#3.

We conclude that, in series #2 and #3 glasses, coalescence occurs as bubbles continue to nucleate and the space between neighboring bubbles is sufficiently small. For the three glass series, bubble coalescence is the more strongly marked in the same pressure range (between 100 and 50 MPa P_f), as observed in faster decompression rate experiments (Le Gall and Pichavant 2016).

Bubble size distributions. Each of the three glass series shows a different evolution of the bubble size distribution (Figs. 3 and 4). With decreasing P_f, the BSD of series #1 glasses evolve from a power law (D30#1, P_f = 150 MPa, Figs. 3a and 4a), exponential (D2#1, D22#1, and D5#1, P_f = 100–50 MPa, Fig. 4a) and then to a mixed power law–exponential distribution that is specific of the 25 MPa P_f D24#1 charge. The power law BSD (which was not found in the faster decompression rate experiments, Le Gall and Pichavant 2016) is interpreted to reflect ongoing bubble nucleation and bubble growth. The fact that the small (volumes < 200 μm^3) bubbles are not fitted by the power law suggests that the nucleation process is close to its end. The exponential distributions are interpreted to indicate a mechanism of bubble coalescence that goes along without further bubble nucleation. The mixed power law–exponential

BSD observed at 25 MPa is due to the occurrence of the second bubble nucleation event. The increase in the number of bubbles and sizes when compared to the 50 MPa charge requires either fast bubble growth or a combination of bubble growth and coalescence, possibly promoted by rapid gas expansion between 50 and 25 MPa.

Series #2 glasses are characterized by a continuous evolution from a power law (D1#2 and D2#2, P_f = 150 and 100 MPa, Figs. 3b and 4b) to mixed power law–exponential distributions (D5#2, D6#2, and D8#2, P_f = 50 and 25 MPa, Fig. 4b) upon decreasing P_f. This transition is consistent with a mechanism of bubble growth dominated by coalescence, taking place between P_f = 100 and 50 MPa, as well as by a lowering in the bubble nucleation rate.

Series #3 glasses are characterized by power law, exponential, and mixed power law–exponential bubble size distributions (Figs. 3c and 4c). Exponential distributions first were not found in series #2 and second appear at different P_f in series #3 samples. We interpret this type of BSD to reflect the pre-dominant influence of bubble growth, bubble nucleation playing a relatively minor role. Bubble coalescence would become more important in the case of mixed power law–exponential distributions.

We conclude that power law, exponential and mixed power law–exponential bubble size distributions are observed in all glass series, with the exception of the series #2 glasses that lack exponential BSDs.

Fragmentation. A process of magma fragmentation was observed in a total of three series #1 charges decompressed to 25 MPa P_f (Table 4). D19#1 was recovered entirely as a fine (<500 μm) glass powder and S+D40#1 partially so. D12#1 yielded coarse (<1.5 mm) glass fragments. Two other 25 MPa P_f series #1 charges were unfragmented but yielded strongly unusual textures (extruded foam for D24#1 and extruded dense block for D27#1). Capsule failure was observed systematically in the series #1 charges decompressed to 25 MPa, occurring in four out of the five charges performed under these conditions, despite capsules having lengths up to 5 cm to accommodate gas expansion during decompression. However, capsule failure and fragmentation are not always associated since the capsule of the fragmented D19#1 charge did not fail. When capsules failed, failures were systematically found around the melt cylinders and never in void spaces. Both fragmented and unfragmented charges contain a population of small bubbles (Table 4). Therefore, melt fragmentation in our experiments is intimately associated with the occurrence of the second event of bubble nucleation characterized for charge D24#1. Our experimental observations thus strengthen the proposal (Massol and Koyaguchi 2005) that late nucleation of gas bubbles in the conduit triggers fragmentation. Although detailed discussion of the fragmentation mechanism is outside the scope of this paper, our observations (presence of small bubbles, capsule failures) are consistent with fragmentation being driven by high internal pressures inside the newly formed bubbles (Zhang 1999; Massol and Koyaguchi 2005).

Equilibrium vs. disequilibrium degassing

Chemical equilibrium is reached or approached in the H_2O-only melts (series #1). On the one hand, glasses decompressed to P_f = 200, 150, 100, and 25 MPa have H_2O concentrations in

agreement with their respective solubilities, and thus follow an equilibrium degassing trend (Fig. 5a). On the other hand, deviation from equilibrium is encountered in glasses decompressed to P_f = 60 and 50 MPa (D22#1 and D5#1), which have H_2O concentrations in excess compared to their respective equilibrium solubilities (Fig. 6). H_2O supersaturations of the order of 0.2–0.35 wt% absolute were found in these two glasses. This indicates the possibility of near- or slight non-equilibrium degassing in the H_2O-only melts, which would provide the driving force for the nucleation of the second bubble population observed at 25 MPa. However, and despite chemical equilibrium being approached, textural equilibrium (defined here as the texture that corresponds to an equilibrium vesicularity, the latter theoretically generated by assuming degassing along the equilibrium vesicularity curves, see Fig. 2a and Le Gall and Pichavant 2016) is not attained in the series #1 melts that have vesicularities lower than expected from equilibrium degassing (Fig. 2a). This demonstrates that, to achieve chemical equilibrium, H_2O can be lost diffusively from the melts during decompression, either toward the gas-melt capsule interface, as suggested by the H_2O distribution profiles measured in D22#1 and D5#1 charges (Fig. 6), or toward the gas bubbles present inside the glass cylinder.

In contrast, disequilibrium degassing occurs systematically in the CO_2-bearing melts (series #2 and #3). CO_2 is retained within these melts at elevated concentration levels (Figs. 5b and 5c). In parallel, H_2O is lost in significant amounts, especially in series #2 glasses. The combination of high melt CO_2 concentrations and significant H_2O losses generates a disequilibrium degassing trend. Such a deviation from a closed-system equilibrium decompression trend was previously observed in the experiments of Pichavant et al. (2013) and Le Gall and Pichavant (2016) and modeled using a diffusive fractionation mechanism by Yoshimura (2015). For series #2, glass CO_2 concentrations are weakly negatively correlated with vesicularities and positively correlated with BNDs. As discussed by Pichavant et al. (2013) and Le Gall and Pichavant (2016), equilibrium degassing in CO_2-bearing melts need both numerous and large bubbles, i.e., high vesicularities, which is the case neither in our series #2 nor in our series #3 post-decompression glasses.

Effect of decompression rate on degassing mechanisms

Previous experiments on hydrated rhyolites and phonolites (Mangan and Sisson 2000; Mourtada-Bonnefoi and Laporte 2004; Iacono-Marziano et al. 2007; Cluzel et al. 2008) have demonstrated strong variations in bubble number density, bubble size and vesicularity with decompression rates, as anticipated on the basis of numerical simulations (Toramaru 1995, 2006). In line with these observations, below we compare our experimental products with those from the experiments of Le Gall and Pichavant (2016) performed at a higher decompression rate of 78 kPa/s (or 3 m/s), under the same conditions and on compositions similar to those in this study. The comparison is focused on the series #2 glasses and it is extended to the experimental products from the experiments of Pichavant et al. (2013) performed at lower decompression rates (17 and 27 kPa/s, or 0.64 and 1.03 m/s) under similar conditions and compositions.

First, a positive correlation between bubble number density and decompression rate (dP/dt) is generally observed. For a given P_f,

the experiments decompressed the most rapidly have the highest BNDs (Fig. 7a). Note that the data points for the two slowest decompression rates (17 and 27 kPa/s) are for 1150 °C experiments, whereas experiments for the two fastest decompression rates (39 and 78 kPa/s) are performed at 1200 °C. The positive correlation between decompression rate and BND results from timescales for bubble growth and coalescence becoming shorter and volatile supersaturations larger when dP/dt is increased. Both effects would promote the nucleation of new bubbles, and so increase the BNDs. The general positive correlation found in this study is consistent with previous results on rhyolitic systems (e.g., Mourtada-Bonnefoi and Laporte 2004; Cluzel et al. 2008). However, our experimental results show more variability. For a given decompression rate, no stationary BND value is reached and BND depends in a complex way on P_f (Fig. 2c; Le Gall and Pichavant 2016) and on the combination between nucleation (marked by two events for the CO_2-free melts and continuous for the CO_2-bearing melts), growth (coalescence) processes, and outgassing. Therefore, application of BNDs to infer magma ascent rates (Toramaru 2006) needs caution in the case of basaltic melts.

Average bubble diameters for the series #2 glasses show little variations with $dP/dt > 25$ kPa/s (Fig. 7b). The 25 MPa P_f data points have D slightly negatively correlated with dP/dt, whereas the trends for the 50 MPa P_f range from negative to slightly positive. Below 25 kPa/s, significant variations in bubble diameters are observed at 1150 °C (Fig. 7b). This is interpreted to reflect the predominant role of bubble growth since bubble growth and maybe coalescence would be favored by lowering dP/dt (e.g., Mangan and Sisson 2000). Vesicularities are constant or generally slightly decrease with decreasing dP/dt (Fig. 7c). These variations reflect the combined influences of the bubble diameter (whose increase below 25 kPa/s contributes to a vesicularity increase) and of the BND (whose decrease with decreasing dP/dt contributes to lowering the number of bubbles).

Previous works in rhyolitic systems have suggested a very small effect of decompression rate on nucleation pressure (Mourtada-Bonnefoi and Laporte 2004; Cluzel et al. 2008). In our experiments on basaltic compositions, a significant difference in nucleation pressure is found in the case of our series #2 glasses, ΔP_{HoN} being lower (≤50 MPa, this study) at 39 than at 78 kPa/s (<100 MPa, Le Gall and Pichavant 2016). This difference in nucleation pressure cannot be attributed to heterogeneous bubble nucleation since D1#2 (Table 3), one of the charges examined by SEM, showed a large population of homogeneously distributed bubbles. It is possible that the higher ΔP_{HoN} measured at 78 kPa/s results from a higher glass CO_2 concentration (901 ± 104 ppm, Le Gall and Pichavant 2016) than in D1#2 (818 ± 111 ppm, Table 3). However, as mentioned above, bubbles in the 39 kPa/s charge could have started to nucleate at pressures below than but close to 150 MPa, which would lead to similar supersaturation pressures in the two studies ($\Delta P_{HoN} \approx 50$ MPa).

VOLCANOLOGICAL IMPLICATIONS

Comparison between experimental and Strombolian textural parameters

Despite the fact that our experimental products do not simulate the last stages of degassing near the surface and post-
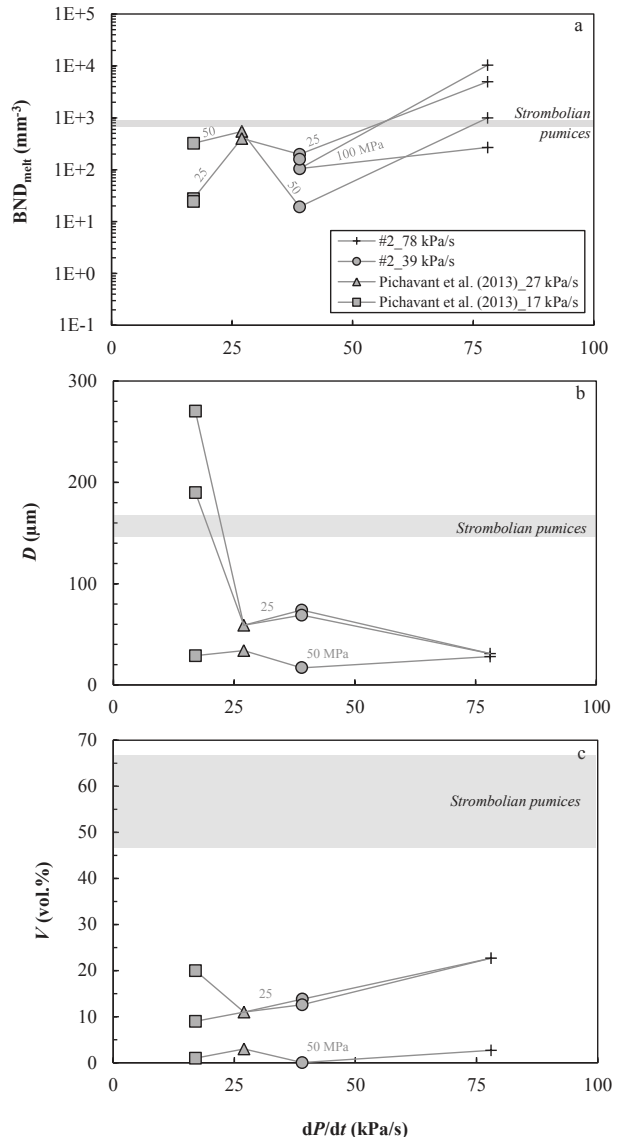

FIGURE 7. (a) Bubble number density per unit volume of melt BND_{melt}, **(b)** average bubble diameter D, and **(c)** vesicularity V plotted as a function of decompression rate for the series #2 glasses. Textural data from this study ($dP/dt = 39$ kPa/s, Table 3) are compared with data from Le Gall and Pichavant (2016, $dP/dt = 78$ kPa/s) and from Pichavant et al. (2013, $dP/dt = 17$ and 27 kPa/s). The BND, D, and V values for Strombolian pumices (data come from Polacci et al. 2006, 2009) are shown for comparison. The gray continuous lines are P_f isobars drawn for $P_f = 100$, 50, and 25 MPa.

fragmentation processes, the comparison of bubble textures in our H_2O-CO_2-bearing melts decompressed at 39 kPa/s (or 1.5 m/s, series #2 from this study) and in Strombolian explosive samples can provide insights on degassing processes occurring in the Stromboli volcanic conduit. The comparison focuses on pumices from paroxysmal explosive activity, as well as on scoriae from normal explosive activity (Polacci et al. 2006, 2009) although it is clear that the two systems correspond to two contrasted degassing regimes. At $P_f = 25$ MPa (i.e., at the pressure

corresponding to the shallower depth in our experiments), the series #2 charges show a narrow range of bubble sizes ranging from 21–24 to 175–179 μm (Table 3). For comparison, the pumice samples have a similar minimum bubble size (21–23 μm) but a larger maximum bubble size around 1 mm (Polacci et al. 2009). From our results, the smaller bubbles would result from a mechanism of continuous nucleation. The absence of bubbles <10 μm in pumices suggests that nucleation ended before magma fragmentation. The large bubble sizes in pumices would result from a combination of growth and coalescence processes in the conduit. These large bubbles have spherical to subspherical shapes. Coalescence is limited during paroxysmal activity as shown by the lack of connected bubbles in both our series #2 melts and in pumice samples. In contrast, connected bubbles occur in scoriae in the form of large coalescing bubbles from 0.5 up to 1.2 mm (Polacci et al. 2009).

The series #2 glasses have vesicularities that extend up to 13.8%, i.e., well below the vesicularities measured in Strombolian eruptive products. For comparison, vesicularities of pumices range from 47 to 67% (Polacci et al. 2006; Fig. 2a) and those of scoriae range between 24 and 78% (Polacci et al. 2006, 2008, 2009). Nevertheless, because a rapid vesicularity increase is observed between 50 and 25 MPa P_f, it is reasonable to expect that vesicularities typical of Strombolian explosive products can be attained by extrapolating the data to $P_f \ll 25$ MPa, i.e., by postulating a fragmentation level shallower than ~1 km.

Strombolian pumices have bubble number densities (6–9 × 10^2 mm^{-3}, Polacci et al. 2009; Fig. 2c) higher by 0.5 order of magnitude than the series #2 melts at 25 MPa P_f (up to 2 × 10^2 mm^{-3}, Fig. 2c). Nevertheless, the BNDs measured in series #2 are in the same range as the BNDs measured in scoriae (1–4.6 × 10^2 mm^{-3}, Polacci et al. 2009). It is reminded here that the bubble nucleation process is continuous in our series #2 melts and that CO_2-supersaturated melt compositions are obtained at 25 MPa P_f. This suggests the possibility that additional bubble nucleation can take place below 25 MPa, which would result in experimental BND becoming closer to the range found in pumices.

BSDs in both our series #2 melts and pumice samples (Fig. 4b) can be fitted by mixed power law–exponential distribution, with power law exponents of 1.51 and 1.96 (this study) and up to 1.4 (Polacci et al. 2009). In contrast, the BSDs of scoriae follow power law trends with exponents of 1 ± 0.2 (Bai et al. 2008; Polacci et al. 2009). From our results, the mixed power law–exponential distributions found in Strombolian pumices would be indicative of a system where growth and coalescence are superimposed on a continuous bubble nucleation mechanism, as the system evolves toward equilibrium (compare with Polacci et al. 2009). The power law distributions found in scoriae would also result from a combination of continuous bubble nucleation and coalescence, in agreement with previous interpretation (Polacci et al. 2009). The decrease in the power law exponent between pumices and scoriae reflects the pre-dominant influence of coalescence in the latter.

Series #2 melts decompressed between 200 and 25 MPa have CO_2 and H_2O concentrations both in the range of Stromboli embayments and melt inclusions data (Fig. 8). Series #2 melts from this study and decompressed at a faster rate (Le Gall and Pichavant 2016) overlap. The agreement between the experimental
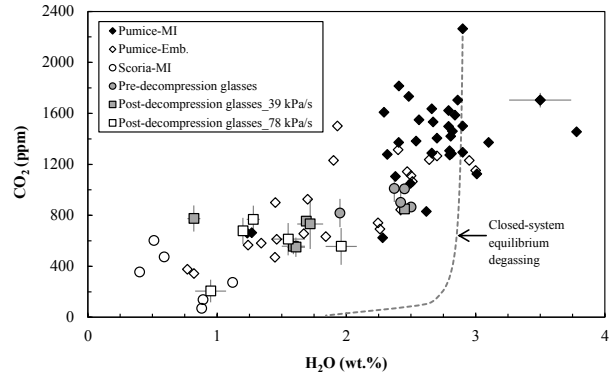

FIGURE 8. H_2O and CO_2 contents in natural glasses from Stromboli (data from Métrich et al. 2010) and comparison with experimental series #2 glasses from this study (39 kPa/s, Table 5) and from Le Gall and Pichavant (2016, 78 kPa/s). Stromboli glasses plotted include melt inclusions (MI) and embayments (Emb.) from pumices and scoriae. Experimental glasses include pre- (circles) and post-decompression glasses (squares). The closed system equilibrium degassing trend (dashed curve) is calculated using VolatileCalc (Newman and Lowenstern 2002).

and analytical data strongly suggests that the natural Stromboli degassing trend is simulated (Pichavant et al. 2013).

We conclude that our decompression experiments on series #2 melts either reproduce or approach certain critical aspects of the natural textures (BNDs, bubble sizes, shapes, and distributions) and chemistries (residual volatile concentrations) of Stromboli explosive basaltic eruptions. The main differences between experimental and natural products concern the maximum bubble sizes and the vesicularities (both lower in the experiments), but the range of natural characteristics is expected to be approached in experiments at P_f below 25 MPa.

Implications for the dynamics of magma ascent at Stromboli volcano

Timescales of magma ascent at Stromboli are poorly constrained yet this is critical information for volcanic risk mitigation. On the one hand, slow geophysically derived ascent rates (3 mm/s, Calvari et al. 2011) have been proposed, leading to unrealistically large timescales of magma transport to the surface (~30 days). On the other hand, the petrologic constraints lead to timescales for ascent of volatile-rich magmas at the origin of paroxysms (Bertagnini et al. 2003; Métrich et al. 2005) that are much shorter, of the order of minutes to hours (<10 h, equivalent to ascent rates >0.21 m/s). In this context, Polacci et al. (2009) used the experimental data of Baker et al. (2006) and Bai et al. (2008) to suggest timescales from "minutes to hours" for bubble size distributions to evolve from power law to mixed power law–exponential. In our experiments, such a transition was observed to take place at a minimum pressure of 50 MPa both for a decompression rate of 1.5 (this study) and 3 m/s (Le Gall and Pichavant 2016). This implies that timescales of 32 (3 m/s) to 64 (1.5 m/s) minutes maximum would be needed to start producing mixed power law–exponential BSDs. These texturally based constraints are in the lower range of timescales estimated from petrological studies.

Additional constraints are provided by the D and BND data

(Fig. 9). The range of natural average bubble sizes and BNDs in Strombolian pumices is bracketed by experiments from this study, Le Gall and Pichavant (2016) and Pichavant et al. (2013). In detail, the 3 m/s experiments on series #2 melts produce BNDs that exceed the natural values. Note, however, that the associated bubble sizes are far too small compared to the natural pumices. Taking 3 m/s as an upper range of ascent rates, timescales of 43 min for "golden" pumice magma to ascend from their source region at 7–8 km depth to the surface are obtained. The 1.5 m/s experiments do not yield BNDs as high as the natural values, although higher experimental BNDs would be expected for P_f below 25 MPa. Therefore, an ascent rate of 1.5 m/s, corresponding to a timescale of 86 min for "golden" pumice magma ascent, also seems plausible. The 1 m/s experiments produce BNDs very close to the natural range both at 25 and 50 MPa P_f. For this decompression rate and below, we observe a decrease of BND with decreasing P_f, interpreted to reflect the pre-dominant influences of bubble growth and coalescence. Below 1 m/s (0.64 m/s), experimental BNDs are lower than natural values.
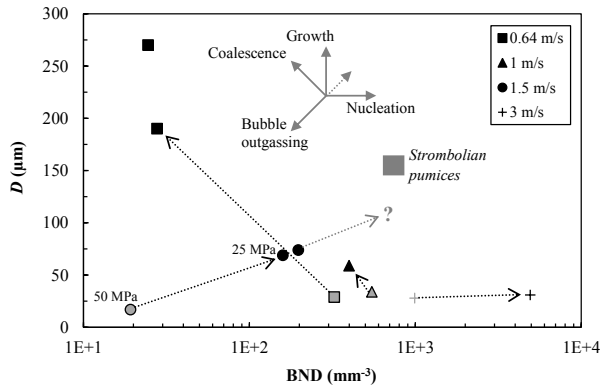
Both the 1 and 0.64 m/s 25 MPa P_f samples are characterized by equilibrium degassing, implying that the driving force for increasing BNDs has been lost. We therefore propose 1 m/s as the lower end of the range of ascent rates at Stromboli, corresponding to ascent timescales of 128 min. In conclusion, use of our experimental D-BND systematics enable the ascent rate of the "golden" pumice magma emitted during paroxysms to be constrained between 1 and 3 m/s.

FIGURE 9. Comparison between textural parameters for natural (Stromboli basaltic pumices) and experimental samples decompressed at various ascent rates. Source of data: natural samples, Polacci et al. (2006, 2009); experimental samples, this study (series #2 glasses, 1.5 m/s, circles, Table 3), Le Gall and Pichavant (2016, 3 m/s, crosses), Pichavant et al. (2013; 0.64 and 1 m/s, squares and triangles, respectively). Average bubble diameters D are plotted as a function of bubble number densities BNDs. The arrows indicate the direction of evolution of the textural parameters from 50 (gray symbols) to 25 MPa P_f (black symbols). Notice that for ascent rates of 1.5 and 3 m/s, the evolution is positive (D increases along with BND from 50 to 25 MPa), whereas for ascent rates <1.5 m/s the evolution is negative. The arrow with a question mark extending the 1.5 m/s trend illustrates the possible evolution of textural parameters at P_f below 25 MPa. The respective influences of the different possible degassing mechanisms (bubble nucleation, growth, coalescence, and outgassing) on textural parameters are indicated. Ascent rates of 1, 1.5, and 3 m/s yield experimental samples with bubble sizes lower than in Strombolian pumices. However, for the 1.5 and 3 m/s data points further evolution (either bubble nucleation, growth, and coalescence, or their combination) below 25 MPa P_f would make it possible to approach the textural characteristics of the pumices. In contrast, volatile supersaturation is absent in both the 1 and 0.64 m/s 25 MPa P_f samples, and so there is no longer a driving force for further nucleation and BND to reach the natural values. In addition, the 0.64 m/s 25 MPa P_f charges have bubble sizes higher than in Strombolian pumices. Consequently, ascent rates >1 m/s are necessary to approach the characteristics of the Strombolian pumices.

REFERENCES CITED

Abràmoff, M.D., Magalhães, P.J., and Ram, S.J. (2004) Image processing with ImageJ. Biophotonics International, 11, 36–43.

Aiuppa, A., Federico, C., Giudice, G., Giuffrida, G., Guida, R., Gurrieri, S., Liuzzo, M., Moretti, R., and Papale, P. (2009) The 2007 eruption of Stromboli volcano: Insights from real-time measurement of the volcanic gas plume CO_2/SO_2 ratio. Journal of Volcanology and Geothermal Research, 182, 221–230 (DOI:10.1016/j.jvolgeores.2008.09.013).

Aiuppa, A., Bertagnini, A., Métrich, N., Moretti, R., Di Muro, A., Liuzzo, M., and Tamburello, G. (2010a) A model of degassing for Stromboli volcano. Earth and Planetary Science Letters, 295, 195–204 (DOI:10.1016/j.epsl.2010.03.040).

Aiuppa, A., Burton, M., Caltabiano, T., Giudice, G., Guerrieri, S., Liuzzo, M., Murè, F., and Salerno, G. (2010b) Unusually large magmatic CO_2 gas emissions prior to a basaltic paroxysm: CO_2 gas emissions prior to a paroxysm. Geophysical Research Letters, 37, L17303 (DOI:10.1029/2010GL043837).

Aiuppa, A., Burton, M., Allard, P., Caltabiano, T., Giudice, G., Gurrieri, S., Liuzzo, M., and Salerno, G. (2011) First observational evidence for the CO_2-driven origin of Stromboli's major explosions. Solid Earth, 2, 135–142 (DOI:10.5194/se-2-135-2011).

Allard, P. (2010) A CO_2-rich gas trigger of explosive paroxysms at Stromboli basaltic volcano, Italy. Journal of Volcanology and Geothermal Research, 189, 363–374 (DOI:10.1016/j.jvolgeores.2009.11.018).

Bai, L., Baker, D.R., and Rivers, M. (2008) Experimental study of bubble growth in Stromboli basalt melts at 1 atm. Earth and Planetary Science Letters, 267, 533–547 (DOI:10.1016/j.epsl.2007.11.063).

Baker, D.R., Lang, P., Robert, G., Bergevin, J.-F., Allard, E., and Bai, L. (2006) Bubble growth in slightly supersaturated albite melt at constant pressure. Geochimica et Cosmochimica Acta, 70, 1821–1838.

Barberi, F., Rosi, M., and Sodi, A. (1993) Volcanic hazard assessment at Stromboli based on review of historical data. Acta Vulcanologica, 3, 173–187.

Bertagnini, A., Métrich, N., Landi, P., and Rosi, M. (2003) Stromboli volcano (Aeolian Archipelago, Italy): An open window on the deep-feeding system of a steady state basaltic volcano. Journal of Geophysical Research, 108 (B7), 2336 (DOI:10.1029/2002JB002146).

Bertagnini, A., Métrich, N., Francalanci, L., Landi, P., Tommasini, S., and Conticelli, S. (2008) Volcanology and magma geochemistry of the present-day activity: constraints on the feeding system. In S. Calvari, S. Inguaggiato, G. Puglisi, M. Ripepe, and M. Rosi, Eds., Learning from Stromboli. American Geophysical Union, Washington, Geophysical Monograph, 182, 19–38.

Bertagnini, A., Roberto, A., and Pompilio, M. (2011) Paroxysmal activity at Stromboli: lessons from the past. Bulletin of Volcanology, 73, 1229–1243 (DOI:10.1007/s00445-011-0470-3).

Blower, J.D., Keating, J.P., Mader, H.M., and Phillips, J.C. (2001) Inferring volcanic degassing processes from vesicle size distributions. Geophysical Research Letters, 28, 347–350.

——— (2002) The evolution of bubble size distributions in volcanic eruptions. Journal of Volcanology and Geothermal Research, 120, 1–23.

Bottinga, Y., and Javoy, M. (1990) MORB degassing: Bubble growth and ascent. Chemical Geology, 81, 255–270.

Bourgue, E., and Richet, P. (2001) The effects of dissolved CO_2 on the density and viscosity of silicate melts: a preliminary study. Earth and Planetary Science Letters, 193, 57–68.

Burgisser, A., Alletti, M., and Scaillet, B. (2015) Simulating the behavior of volatiles belonging to the C–O–H–S system in silicate melts under magmatic conditions with the software D-Compress. Computers & Geosciences, 79, 1–14.

Burton, M., Allard, P., Mure, F., and La Spina, A. (2007) Magmatic gas composition reveals the source depth of slug-driven Strombolian explosive activity.

Science, 317, 227–230 (DOI:10.1126/science.1141900).

Calvari, S., Spampinato, L., Bonaccorso, A., Oppenheimer, C., Rivalta, E., and Boschi, E. (2011) Lava effusion—A slow fuse for paroxysms at Stromboli volcano? Earth and Planetary Science Letters, 301, 317–323.

Cashman, K.V., and Sparks, R.S.J. (2013). How volcanoes work: A 25 year perspective. Geological Society of America Bulletin, 125, 664–690.

Castro, J.M., Burgisser, A., Schipper, C.I., and Mancini, S. (2012) Mechanisms of bubble coalescence in silicic magmas. Bulletin of Volcanology, 74, 2339–2352.

Cluzel, N., Laporte, D., Provost, A., and Kannewischer, I. (2008) Kinetics of heterogeneous bubble nucleation in rhyolitic melts: implications for the number density of bubbles in volcanic conduits and for pumice textures. Contributions to Mineralogy and Petrology, 156, 745–763 (DOI:10.1007/s00410-008-0313-1).

Di Carlo, I., Pichavant, M., Rotolo, S.G., and Scaillet, B. (2006). Experimental crystallization of a high-K arc basalt: The Golden Pumice, Stromboli Volcano (Italy). Journal of Petrology, 47, 1317–1343 (DOI:10.1093/petrology/egl011).

Dixon, J.E., and Pan, V. (1995) Determination of the molar absorptivity of dissolved carbonate in basanitic glass. American Mineralogist, 80, 1339–1342.

Dixon, J.E., Stolper, E.M., and Holloway, J.R. (1995) An experimental study of water and carbon dioxide solubilities in mid-ocean ridge basaltic liquids. Part I: Calibration and solubility models. Journal of Petrology, 36, 1607–1631.

Edmonds, M. (2008) New geochemical insights into volcanic degassing. Philosophical Transactions of the Royal Society A: Mathematical, Physical and Engineering Sciences, 366, 4559–4579 (DOI:10.1098/rsta.2008.0185).

Francalanci, L., Manetti, P., and Peccerillo, A. (1989) Volcanological and magmatological evolution of Stromboli volcano (Aeolian Islands): the roles of fractional crystallization, magma mixing, crustal contamination and source heterogeneity. Bulletin of Volcanology, 51, 355–378.

Francalanci, L., Taylor, S.R., McCulloch, M.T., and Woodhead, J.D. (1993) Geochemical and isotopic variations in the calc-alkaline rocks of Aeolian arc, southern Tyrrhenian Sea, Italy: constraints on magma genesis. Contributions to Mineralogy and Petrology, 113, 300–313.

Francalanci, L., Tommasini, S., and Conticelli, S. (2004) The volcanic activity of Stromboli in the 1906–1998 AD period: mineralogical, geochemical and isotope data relevant to the understanding of the plumbing system. Journal of Volcanology and Geothermal Research, 131, 179–211 (DOI:10.1016/S0377-0273(03)00362-7).

Gaonac'h, H., Stix, J., and Lovejoy, S. (1996) Scaling effects on vesicle shape, size and heterogeneity of lavas from Mount Etna. Journal of Volcanology and Geothermal Research, 74, 131–153.

Gardner, J.E., and Ketcham, R.A. (2011) Bubble nucleation in rhyolite and dacite melts: temperature dependence of surface tension. Contributions to Mineralogy and Petrology, 162, 929–943 (DOI:10.1007/s00410-011-0632-5).

Gardner, J.E., and Webster, J.D. (2016) The impact of dissolved CO_2 on bubble nucleation in water-poor rhyolite melts. Chemical Geology, 420, 180–185.

Gardner, J.E., Hilton, M., and Carroll, M.R. (1999) Experimental constraints on degassing of magma: isothermal bubble growth during continuous decompression from high pressure. Earth and Planetary Science Letters, 168, 201–218.

Gonnermann, H., and Manga, M. (2005) Nonequilibrium magma degassing: Results from modeling of the ca. 1340 A.D. eruption of Mono Craters, California. Earth and Planetary Science Letters, 238, 1–16 (DOI:10.1016/j.epsl.2005.07.021).

——— (2007) The fluid mechanics inside a volcano. Annual Review of Fluid Mechanics, 39, 321–356.

Hurwitz, S., and Navon, O. (1994) Bubble nucleation in rhyolitic melts: Experiments at high pressure, temperature, and water content. Earth and Planetary Science Letters, 122, 267–280.

Iacono-Marziano, G., Schmidt, B.C., and Dolfi, D. (2007) Equilibrium and disequilibrium degassing of a phonolitic melt (Vesuvius AD 79 "white pumice") simulated by decompression experiments. Journal of Volcanology and Geothermal Research, 161, 151–164 (DOI:10.1016/j.jvolgeores.2006.12.001).

Iacono-Marziano, G., Morizet, Y., Le Trong, E., and Gaillard, F. (2012) New experimental data and semi-empirical parameterization of H_2O–CO_2 solubility in mafic melts. Geochimica et Cosmochimica Acta, 97, 1–23 (DOI:10.1016/j.gca.2012.08.035).

Khitarov, N.I., Lebedev, E.B., Dorfman, A.M., and Bagdasarov, N.S. (1979) Effect of temperature, pressure and volatiles on the surface tension of molten basalt. Geochemistry International, 16, 78–86.

La Spina, A., Burton, M.R., Harig, R., Mure, F., Rusch, P., Jordan, M., and Caltabiano, T. (2013) New insights into volcanic processes at Stromboli from Cerberus, a remote-controlled open-path FTIR scanner system. Journal of Volcanology and Geothermal Research, 249, 66–76.

Landi, P., Métrich, N., Bertagnini, A., and Rosi, M. (2004) Dynamics of magma mixing and degassing recorded in plagioclase at Stromboli (Aeolian Archipelago, Italy). Contributions to Mineralogy and Petrology, 147, 213–227 (DOI:10.1007/s00410-004-0555-5).

Lange, R.A. (1994) The effect of H_2O, CO_2, and F on the density and viscosity of silicate melts. Reviews in Mineralogy, 30, 331–369.

Lautze, N.C., and Houghton, B.F. (2007) Linking variable explosion style and magma textures during 2002 at Stromboli volcano, Italy. Bulletin of Volcanology, 69, 445–460.

Le Gall, N. (2015) Basaltic magma ascent and degassing—Experimental approach, 318 p. Ph.D. thesis, University of Orléans.

Le Gall, N., and Pichavant, M. (2016) Homogeneous bubble nucleation in H_2O- and H_2O-CO_2-bearing basaltic melts: results of high temperature decompression experiments. Journal of Volcanology and Geothermal Research, in press.

Lensky, N.G., Niebo, R.W., Holloway, J.R., Lyakhovsky, V., and Navon, O. (2006) Bubble nucleation as a trigger for xenolith entrapment in mantle melts. Earth and Planetary Science Letters, 245, 278–288.

Lesne, P., Scaillet, B., Pichavant, M., and Beny, J.-M. (2011a) The carbon dioxide solubility in alkali basalts: an experimental study. Contributions to Mineralogy and Petrology, 162, 153–168.

Lesne, P., Scaillet, B., Pichavant, M., Iacono-Marziano, G., and Beny, J.-M. (2011b) The H_2O solubility of alkali basaltic melts: an experimental study. Contributions to Mineralogy and Petrology, 162, 133–151.

Lyakhovsky, V., Hurwitz, S., and Navon, O. (1996) Bubble growth in rhyolitic melts: experimental and numerical investigation. Bulletin of Volcanology, 58, 19–32.

Mangan, M.T., and Cashman, K.V. (1996) The structure of basaltic scoria and reticulite and inferences for vesiculation, foam formation, and fragmentation in lava fountains. Journal of Volcanology and Geothermal Research, 73, 1–18.

Mangan, M., and Sisson, T. (2000) Delayed, disequilibrium degassing in rhyolite magma: decompression experiments and implications for explosive volcanism. Earth and Planetary Science Letters, 183, 441–455.

——— (2005) Evolution of melt-vapor surface tension in silicic volcanic systems: Experiments with hydrous melts. Journal of Geophysical Research, 110, B01202.

Martel, C., and Iacono-Marziano, G. (2015) Timescales of bubble coalescence, outgassing, and foam collapse in decompressed rhyolitic melts. Earth and Planetary Science Letters, 412, 173–185.

Massol, H., and Koyaguchi, T. (2005) The effect of magma flow on nucleation of gas bubbles in a volcanic conduit. Journal of Volcanology and Geothermal Research, 143, 69–88.

Mercalli, G. (1907) Vulcani attivi della Terra. Ulrico Hoepli.

Métrich, N., Bertagnini, A., Landi, P., and Rosi, M. (2001) Crystallization driven by decompression and water loss at Stromboli volcano (Aeolian Islands, Italy). Journal of Petrology, 42, 1471–1490.

Métrich, N., Allard, P., Spilliaert, N., Andronico, D., and Burton, M. (2004) 2001 flank eruption of the alkali-and volatile-rich primitive basalt responsible for Mount Etna's evolution in the last three decades. Earth and Planetary Science Letters, 228, 1–17.

Métrich, N., Bertagnini, A., Landi, P., Rosi, M., and Belhadj, O. (2005) Triggering mechanism at the origin of paroxysms at Stromboli (Aeolian Archipelago, Italy): the 5 April 2003 eruption. Geophysical Research Letters, 32, L103056 (DOI:10.1029).

Métrich, N., Bertagnini, A., and Di Muro, A. (2010) Conditions of magma storage, degassing and ascent at Stromboli: new insights into the volcano plumbing system with inferences on the eruptive dynamics. Journal of Petrology, 51, 603–626.

Misiti, V., Vetere, F., Mangiacapra, A., Behrens, H., Cavallo, A., Scarlato, P., and Dingwell, D.B. (2009) Viscosity of high-K basalt from the 5th April 2003 Stromboli paroxysmal explosion. Chemical Geology, 260, 278–285.

Mourtada-Bonnefoi, C.C., and Laporte, D. (1999) Experimental study of homogeneous bubble nucleation in rhyolitic magmas. Geophysical Research Letters, 26, 3505–3508.

——— (2002) Homogeneous bubble nucleation in rhyolitic magmas: an experimental study of the effect of H_2O and CO_2. Journal of Geophysical Research, 107, ECV 2-1–EVC 2-19 (DOI:10.1029/2001JB000290).

——— (2004) Kinetics of bubble nucleation in a rhyolitic melt: an experimental study of the effect of ascent rate. Earth and Planetary Science Letters, 218, 521–537.

Newman, S., and Lowenstern, J.B. (2002) VolatileCalc: a silicate melt–H_2O–CO_2 solution model written in Visual Basic for Excel. Computers & Geosciences, 28, 597–604.

Papale, P., Moretti, R., and Barbato, D. (2006) The compositional dependence of the saturation surface of H_2O+CO_2 fluids in silicate melts. Chemical Geology, 229, 78–95.

Pichavant, M., Di Carlo, I., Le Gac, Y., Rotolo, S.G., and Scaillet, B. (2009) Experimental constraints on the deep magma feeding system at Stromboli volcano, Italy. Journal of Petrology, 50, 601–624.

Pichavant, M., Pompilio, M., D'Oriano, C., and Di Carlo, I. (2011) Petrography, mineralogy and geochemistry of a primitive pumice from Stromboli: implications for the deep feeding system. European Journal of Mineralogy, 23, 499–517.

Pichavant, M., Di Carlo, I., Rotolo, S.G., Scaillet, B., Burgisser, A., Le Gall, N., and Martel, C. (2013) Generation of CO_2-rich melts during basalt magma ascent and degassing. Contributions to Mineralogy and Petrology, 166, 545–561.

Polacci, M., Baker, D.R., Mancini, L., Tromba, G., and Zanini, F. (2006) Three-dimensional investigation of volcanic textures by X-ray microtomography

and implications for conduit processes. Geophysical Research Letters, 33, L13312 (DOI:10.1029/2006GL026241).

Polacci, M., Baker, D.R., Bai, L., and Mancini, L. (2008) Large vesicles record pathways of degassing at basaltic volcanoes. Bulletin of Volcanology, 70, 1023–1029.

Polacci, M., Baker, D.R., Mancini, L., Favretto, S., and Hill, R.J. (2009) Vesiculation in magmas from Stromboli and implications for normal Strombolian activity and paroxysmal explosions in basaltic systems. Journal of Geophysical Research, 114, B01206 (DOI:10.1029/2008JB005672).

Proussevitch, A.A., Sahagian, D.L., and Tsentalovich, E.P. (2007) Statistical analysis of bubble and crystal size distributions: Formulations and procedures. Journal of Volcanology and Geothermal Research, 164, 95–111.

Richet, P., Whittington, A., Holtz, F., Behrens, H., Ohlhorst, S., and Wilke, M. (2000) Water and the density of silicate glasses. Contributions to Mineralogy and Petrology, 138, 337–347.

Ripepe, M., and Harris, A.J. (2008) Dynamics of the 5 April 2003 explosive paroxysm observed at Stromboli by a near-vent thermal, seismic and infrasonic array. Geophysical Research Letters, 35, L07306 (DOI:10.1029/2007GL032533).

Rosi, M., Bertagnini, A., and Landi, P. (2000) Onset of the persistent activity at Stromboli volcano (Italy). Bulletin of Volcanology, 62, 294–300.

Rosi, M., Pistolesi, M., Bertagnini, A., Landi, P., Pompilio, M., and Di Roberto, A. (2013) Stromboli volcano, Aeolian Islands (Italy): present eruptive activity and hazards. Geological Society, London, Memoirs, 37, 473–490.

Scaillet, B., Pichavant, M., Roux, J., Humbert, G., and Lefèvre, A. (1992) Improvements of the Shaw membrane technique for measurement and control of f_{H_2} at high temperatures and pressures. American Mineralogist, 77, 647–655.

Shishkina, T.A., Botcharnikov, R.E., Holtz, F., Almeev, R.R., and Portnyagin, M.V. (2010) Solubility of H_2O-and CO_2-bearing fluids in tholeiitic basalts at pressures up to 500MPa. Chemical Geology, 277, 115–125.

Sparks, R.S.J. (2003) Dynamics of magma degassing. Geological Society, London, Special Publications, 213, 5–22.

Taylor, J.R., Wall, V.J., and Pownceby, M.I. (1992) The calibration and application of accurate redox sensors. American Mineralogist, 77, 284–295.

Toramaru, A. (1995) Numerical study of nucleation and growth of bubbles in viscous magmas. Journal of Geophysical Research, 100, 1913–1931.

——— (2006) BND (bubble number density) decompression rate meter for explosive volcanic eruptions. Journal of Volcanology and Geothermal Research, 154, 303–316.

Vetere, F., Behrens, H., Misiti, V., Ventura, G., Holtz, F., De Rosa, R., and Deubener, J. (2007) The viscosity of shoshonitic melts (Vulcanello Peninsula, Aeolian Islands, Italy): insight on the magma ascent in dikes. Chemical Geology, 245, 89–102.

Woods, A.W., and Koyaguchi, T. (1994) Transitions between explosive and effusive eruptions of silicic magmas. Nature, 370, 641–644.

Yoshimura, S. (2015) Diffusive fractionation of H_2O and CO_2 during magma degassing. Chemical Geology, 411, 172–181.

Zhang, Y. (1999) A criterion for the fragmentation of bubbly magma based on brittle failure theory. Nature, 402, 648–650.

Zhang, Y., and Ni, H. (2010) Diffusion of H, C, and O components in silicate melts. Reviews in Mineralogy and Geochemistry, 72, 171–225.

APPENDIX

Surface tensions (σ) have been calculated from our experimentally determined supersaturation pressures (ΔP_{HoN}) and nucleation rates (J) computed from our measured bubble number densities and decompression timescales. Strictly speaking our calculations consider only water as the sole dissolved volatile, and so are applicable only to series #1 melts. The expression of the critical degree of supersaturation ΔP_{HoN} is given by (e.g., Hurwitz and Navon 1994; Mourtada-Bonnefoi and Laporte 2002):

$$\Delta P_{HoN} = \sqrt{\frac{16 \cdot \pi \cdot \sigma^3}{3 \cdot k \cdot T \cdot \ln\left(\dfrac{J}{J_0}\right)}}$$

where k is the Boltzmann constant (1.38×10^{-23} J/K), T is the temperature (in K) and J_0 is the preexponential nucleation rate (in m^{-3}/s).

The parameter J_0 that is given by (e.g., Mourtada-Bonnefoi and Laporte 2004):

$$J_0 = \frac{\left(2 \cdot \Omega_L \cdot n_0^2 \cdot D\right)}{a_0 \cdot \left(\dfrac{\sigma}{k \cdot T}\right)^{\frac{1}{2}}}$$

where Ω_L is the volume of water molecules in the liquid ($\Omega_L = 3 \times 10^{-29}$ m^3), n_0 is the number of water molecules per unit volume of liquid, a_0 is the mean distance between water molecules ($a_0 \approx n_0^{-1/3}$) and D is the water diffusivity in the liquid, has been estimated. D is taken from the equation of Zhang and Ni (2010) that takes into consideration the effects of H_2O content and temperature. n_0 is defined as $6.02 \times 10^{23} \times X_m \times \rho_{liq}/M$, where 6.02×10^{23} is the Avogadro number, X_m is the mass fraction of molecular water in the liquid, ρ_{liq} is the liquid density (2650 kg/m^3), and M is the molar mass of water (0.018 kg/mol). Ω_L and X_m parameters are poorly constrained in basalt melts and we have used the values given by Mourtada-Bonnefoi and Laporte (2004), determined for rhyolitic liquids. Checks were performed to evaluate their influence on the calculated results and found to be small (<0.001 N/m). In the same way, the choice of the D equation leads to very small (<0.001 N/m) differences in σ.